OPTICAL ENGINEERING OF TITANIUM NITRIDE THIN FILMS FOR NANOPLASMONIC BIOSENSING

by
CEMRE IRMAK KAYALAN

Submitted to the Graduate School of Engineering and Natural Sciences
in partial fulfillment of the requirements for the degree of Master of Science

Sabancı University
December 2021

OPTICAL ENGINEERING OF TITANIUM NITRIDE THIN FILMS FOR NANOPLASMONIC BIOSENSING

APPROVED BY:

Assoc. Prof. Dr. Meral Yüce
(Thesis Supervisor)

Asst. Prof. Dr. Hasan Kurt
(Thesis Co-Supervisor)

Assoc. Prof. Dr. Yılmaz Şimşek

Asst. Prof. Dr. Mehmet Kocatürk

DATE OF APPROVAL: 17/12/2021

ABSTRACT

OPTICAL ENGINEERING OF TITANIUM NITRIDE THIN FILMS FOR NANOPLASMONIC BIOSENSING

CEMRE IRMAK KAYALAN

Materials Science and Nano Engineering, M.Sc. Thesis, December 2021

Thesis Supervisor: Assoc. Prof. Dr. Meral YÜCE

Thesis Co-supervisor: Asst. Prof. Dr. Hasan KURT

Keywords: transition metal nitrides, titanium nitride, noble metals, reactive sputtering

Over the last years, promising concepts and practical approaches of miniaturized devices with remarkable features in the field of plasmonics have drawn a lot of attention. Generally, noble metals have been used in this field due to their high electrical conductivity, tunable plasmon frequencies, and chemical stability. However, they have a barrier for high volume production and for high-performance applications because of their high costs and loss mechanism in visible and near infrared region. Noble metals, like gold and silver, does not allow tunability in their optical properties. Therefore, research has begun to find and improve alternative plasmonic materials to replace noble metals. The transition metal nitrides (TMNs) have been suggested as an alternative for their low cost, chemical stability, and compatibility with biological mediums when compared in the literature for nanoplasmonic biosensing applications. Especially, their plasmonic response can be tuned with nanostructural and stoichiometrical change. This thesis provides brief introduction for detection methods for nanoplasmonic sensing. A lithography approach, nanosphere lithography, is explained for future work in this research due to its simplicity and cost-effectiveness in patterning surfaces towards biosensing applications. Noble metals and TMNs will be compared, particularly suggested titanium nitride (TiN) thin films belonging to the 4B transition metal group in the periodic table. Thin-film fabrication was done under reactive radio-frequency sputtering. This study offers a route for optimization of TiN film fabrication and demonstrates several ways to reduce oxygen contaminant concentration in sputtering. Produced thin films' characterizations were done with energy-dispersive spectroscopy, X-ray diffraction, Raman spectroscopy, four-point probe measurement, variable angle

spectroscopic ellipsometry to evaluate the compositional, electrical, morphological, and optical properties. Room temperature, purging with argon gas, overnight vacuum, and substrate heating sputtering are compared. All three approaches towards decreasing oxygen presence during deposition and enhancing crystollographic structure showed improvement in the conductivity and crystallinity of the thin films.

ÖZET

TİTANYUM NİTRÜR İNCE FİLMLERİN NANOPLAZMONİK BİYOSENSÖR UYGULAMALARI İÇİN OPTİK MÜHENDİSLİĞİ

Cemre Irmak KAYALAN

Malzeme Bilimi ve Nano Mühendislik, Yüksek Lisans Tezi, Aralık 2021

Tez Danışmanı: Doç. Dr. Meral YÜCE

Tez Eş Danışmanı: Dr. Öğr. Üye. Hasan KURT

Anahtar kelimeler: geçiş metal nitrürler, titanyum nitrür, soy metaller, reaktif saçtırma

Son yıllarda, minyatür cihazların umut verici çözümleri ve pratik yaklaşımları dikkat çekerek plazmonik alanında büyük ilgi gördü. Genel olarak, yüksek elektriksel iletkenlikleri, ayarlanabilir plazmon frekansları ve kimyasal kararlılıkları nedeniyle bu alanda soy metaller kullanılmıştır. Ancak görünür ve yakın kızılötesi bölgede yüksek maliyetleri ve kayıp mekanizmaları nedeniyle yüksek hacimli üretim ve yüksek performanslı uygulamalar için engel teşkil ederler. Altın ve gümüş gibi soy metaller, optik özelliklerinde ayarlanabilirliğe izin vermez. Bu nedenle soy metallerin yerini alacak alternatif plazmonik malzemeleri bulmak ve geliştirmek için bir araştırma başlamıştır. Geçiş metali nitrürlerinin (GMN) nanoplazmonik biyosensör uygulamaları için literatürde karşılaştırıldığında düşük maliyet, kimyasal kararlılık, ve biyolojik ortamlarla uyumluluk açısından soy metallere bir alternatif olduğu gösterilmiştir. Özellikle, plazmonik tepkileri nanoyapısal ve stokiyometrik değişim ile ayarlanabilir. Bu tez, nanoplazmonik sensör için algılama yöntemleri ile ilgili giriş bilgisi verir. Bir litografi yaklaşımı olan nanoküre litografisi, bu çalışmanın gelecek planı olan biyosensör uygulamalarına yönelik yüzeylerin modellenmesindeki basitliği ve maliyet etkinliği nedeniyle bu araştırmada açıklanmıştır. Soy metaller ve GMN'ler, özellikle periyodik tablodaki 4B geçiş metal grubuna ait, önerilen titanyum nitrür (TiN) ince filmler karşılaştırılacaktır. İnce film üretimi, reaktif radyo frekansı püskürtme altında yapıldı. Bu çalışma, TiN film üretimi ve püskürtmede gerçekleşen oksijen kontaminasyonunun konsantrasyonunu azaltmanın yolları hakkında optimizasyon bilgisi verir. Üretilen ince filmlerin karakterizasyonları, enerji dağılımlı spektroskopi, X-ışını kırınımı, Raman spektroskopisi, dört nokta temaslı iletkenlik ölçümü, değişken açılı spektroskopik

elipsometri ile bileşimsel, elektriksel, morfolojik ve optik özellikleri değerlendirmek için yapıldı. Oda sıcaklığı, argon gazı ile temizleme ve gece boyunca vakum, alt tabaka ısıtma püskürtme karşılaştırılır. Biriktirme sırasında oksijen varlığının azaltılmasına yönelik üç yaklaşımın tümü, ince filmlerin iletkenliğinde ve kristalliğinde gelişme göstermiştir.

A**CKNOWLEDGEMENTS**

I would like to start by mentioning this thesis covers the result of my five months M.Sc. studies in the ‘House of Research’ group at the research center of Sabanci University, SUNUM. There are many people I would like to express my gratitudes to who helped me during my studies both physically and mentally. I apologize if I forgot to mention any name.

First and foremost, I would like to thank my supervisor, Assoc. Prof. Dr. Meral Yüce for all the guidance, encouragement, and providing me the oppurtunity to be in her group. She believed in me and changed my point of view towards life. I won’t forget the life lessons I have gained from her. The experiences I have earned during the last year will always be an important part of my life.

I want to thank my co-supervisor Assist. Prof. Dr. Hasan Kurt for being the mentor with all the knowledge and skills he shared with me in this challenging project. With this project, I had the possibility to participate in the studies developing in the cleanroom. I am grateful for his enthusiasm and advice during the past months.

My special thanks, but a simple thanks won’t be enough to describe the contributions of Prof. Dr. Mehmet Ali Gülgün and Prof. Dr. Cleva Ow-Yang to me since my second year at the university. They made me realize my inner self and showed me the way to be a better version of myself day by day in my studies and for my life ahead. Mali hoca once said that I carry the ‘Atlas’ in me, which is a sincere and meaningful word for me to hear from him. I am deeply thankful for his support and discussions. I hope our conversations will carry on from where we left.

I cannot express how much I am grateful for those who led me to be who I am during my academic career in this university, starting from my bachelor years, Assoc. Prof. Dr. Özge Akbulut, Prof. Dr. Selmiye Alkan Gürsel, Prof. Dr. Melih Papila, Prof. Dr. Canan Atılgan, Assoc. Prof. Dr. Emre Erdem, Assoc. Prof. Dr. Fevzi Çakmak Cebeci. They have directly and indirectly spend their efforts for me to improve myself.

I would like to thank my lab mates Ayhan Parlar, Parsa Pishva, Semih Pehlivan, Deniz Yılmaz, Fatma Sert, Büşra Gürel, Beyza Günaydın, Eda Çapkın for their friendship, help, and cooperation.

Many thanks to the rest of my friends and beyond friends Tuğçe Akkaş Mohammed Moradi and Omid Mohammed Moradi for always being there for me (my kuşito family), Aysu Yurduşen Öztürk (the reason why I chose materials science), Yelda Yorulmaz, Deniz Köken, Onur Zırhlı, İpek Bilge, Kadriye Kahraman, Senem Seven, Utku Seven, Can Akaoğlu, Lyn Zemberekçi, Aleyna Beste Özhan, Şeyma Burcu Gülşen, Korin Gasia Özkaya, Tuğba Sarı, Ayşe Ay, Atakan Koçanalı, Alp Duman, Ekin Özek (thanks a lot for the support you give for all those countless nights of study), Melih Can Taşdelen, Özberk Öztürk, Osman Şahin, Oğuz Albayrak, Farid Irani, Tuçe Fidan, the people I shared L021, the people who were my assistants during the years, the cleanroom team (Bülent Köroğlu, Selim Tanrısevsin, Ali Osman Çetinkaya, Onur Serbest, Serkan Bostan, Süleyman Çelik) for all the knowledge sharing, fruitful discussions, moral support, nice company, and for any help I received during the years.

I must also give greatest thanks to my deep love and sincere gratitude to my best friend Emre Yılmaz Urcu for all the support, love, patience, and humor that brighten my days, and for bearing with my grumpiness in discouraging times.

Last but not least, my all-time supporters in any way my family; mom, dad, and my dear brother, I appreciate you all for always being the light in my life. I am way beyond lucky to have you. I wouldn't be here today if you weren't by my side. Love you with all my heart!

My grandmother, my next step is to be a 'doctor', not as you wished like a medical doctor, but I think you would be proud.

I would like to acknowledge the support of the Scientific and Technological Research Council of Turkey (TÜBİTAK) received under 1001 project (120F065).

To my beloved family…

TABLE OF CONTENTS

LIST OF FIGURES

LIST OF TABLES

LIST OF ABBREVIATIONS

AC	Alternating current
CL	Colloidal lithography
DC	Direct current
EDS	Energy-dispersive spectroscopy
EM	Electromagnetic
EOT	Extraordinary Optical Transmission
LSP	Localized surface plasmon
LSPR	Localized surface plasmon resonance
NIR	Near infrared region
POC	Point-of-care
RF	Radio Frequency
RI	Refractive Index
SEM	Scanning Electron Microscope
SPP	Surface plasmon polaritons
SPR	Surface plasmon resonance
TMN	Transition metal nitride
VASE	Variable angle spectroscopic ellipsometer
VIS	Visible region
XRD	X-ray diffraction

LIST OF SYMBOLS/NOTATIONS

S_B	Refractive index sensitivity
S_S	Surface sensitivity
$k_{s,d}$	Surface plasmon polariton
k_x	Wavenumber of the surface plasmon
l_d	Electromagnetic field decay constant
ε_d	Dielectric permittivity of dielectric medium
ε_m	Dielectric permittivity of metal medium
ρ_s	Sheet resistance
ω_p	Plasma frequency
d	Distance
k	Extinction coefficient
R_s, R_p	Fresnel coefficients
t	Thickness
θ	Angle of incidence
ω	Angular frequency
c	Speed of light in vacuum
n	Refractive index
λ	Wavelenght

“The goal is not to be perfect by the end.
The goal is to be better today.”

Simon Sinek

1 INTRODUCTION

1.1 Plasmonic Sensing

Plasmonic is a study of electromagnetic (EM) radiation, which is light, interacts with metals and coupling free electrons of the metal as collective oscillations of these free electrons. Surface Plasmons (SPs) are electromagnetic modes created when optical rays are coupled to free electrons in a metal. These plasmonic modes can be induced at the interface between noble metal and a dielectric, and they produce an evanescent field that permeates the surrounding media. When plasmonic devices are utilized as refractometric sensing platforms, this evanescent field is susceptible to changes in refractive index (RI) near the metal surface, functioning as a detecting probe [1], [2]. It can be distinguished into two types of SPs based on their excitation: propagating SPs excited in thin metal films, also known as Surface Plasmon Polaritons (SPPs) or Surface Plasmon Resonance (SPR), and localized SPs excited on sub-wavelength-sized metal nanoparticles, also known as Localized Surface Plasmon Resonance (LSPR). Extraordinary optical transmission (EOT) is the third detection method that is goning to be discussed, based on the interactions of the incident phonons with periodic arrays of nanoholes. This phenomenon employs both SPR and LSPR in one single geometry.

1.1.1 Surface Plasmon and Surface Plasmon Polariton

When light strikes a metal layer at the proper angle and energy, the energy of photons is translated and stored by density fluctuations in conduction electrons, which are known as surface plasmons (SP). Surface plasmons at the metal-dielectric interface propagate as a longitudinal charge-compression electromagnetic wave in surface plasmon polaritons

(SPPs). Figure 1 depicts the layered structure, the most basic geometry for available SPPs. Although both are subwavelength in the distance, the field penetrates more deeply into the dielectric space than the metal, as shown. Surface plasmon polaritons are used in the SPR biosensor. Electromagnetic (EM) waves act like a quasi-free electron plasma and generate an evanescent field at the interface between a thin metal layer and a dielectric. The SPP can be called as transverse-magnetic (TM) mode with an evanescent field distribution parallel to the interface plane. The magnetic vector is perpendicular to the wave propagation direction and parallel to the interface plane.

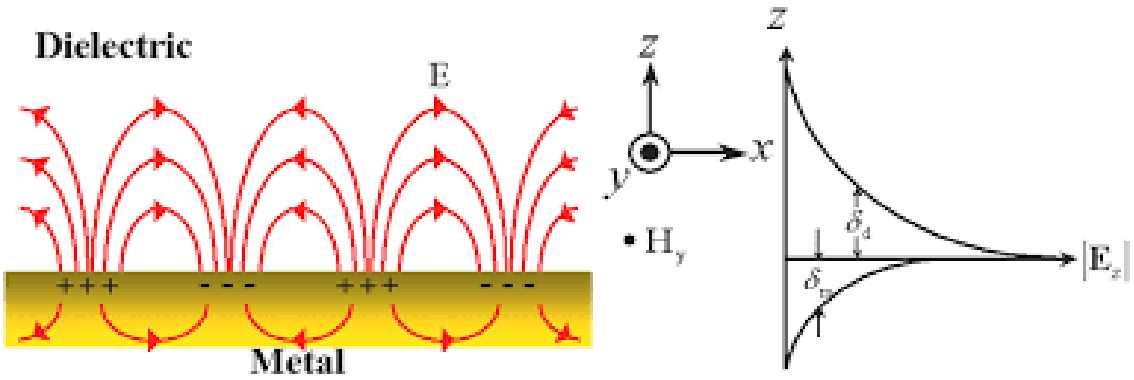

Figure 1 Illustration of SPP between a metal and a dielectric**;** electric field distribution and schematic of SP [3].

SPP can be related to the Maxwell equation due to its property of having a momentum. If the incident photon frequencies are between $0<\omega<\frac{\omega_p}{\sqrt{2}}$, the frequency of incoming energy is ω, plasma frequency is ω_p, the surface-related polaritons can be excited in broad-spectrum [4].

$$k_x^2 = \frac{\varepsilon_m \varepsilon_d}{\varepsilon_m + \varepsilon_d} \cdot \frac{\omega^2}{c^2} \tag{1.1}$$

where ε_m is the dielectric permittivity of metal with free-electron rich medium, ε_d is the dielectric permittivity of a near-dielectric medium, the wavenumber of the surface plasmon constrained to the interface is k_x, the speed of light in a vacuum environment is stated with c. In thin-film layers SPPs can be excited by transverse magnetic or p-polarized incoming waves with the most common planar structure. Either $\varepsilon_m(\omega) \cdot \varepsilon_d(\omega) < 0$ or $\varepsilon_m(\omega) + \varepsilon_d(\omega) < 0$ conditions must be met for the excitement of an

interface-bound SPP. It should be noted that under these circumstances, the standard components of the wave vectors are completely imaginary. SPP includes a momentum component and is characterized using the dispersion relation (DR) derived from the Maxwell equation. The boundary condition for a single planar metal-dielectric interaction proves that the fields are continuous. Calculating the wave number in the propagation direction to ensure the existence of non-zero solutions to the Maxwell equation provides the following:

$$k_x = \frac{\omega}{c}.\sqrt{\frac{\varepsilon(\omega).n^2}{\varepsilon(\omega)+n^2}} \tag{1.2}$$

The above equation shows that wavenumber of surface plasmons, k_x, highly depend on the dielectric function of the metal ε and the refractive index of the surrounding medium n. ε_m denotes the metal's frequency-dependent and complex dielectric function with equation $\varepsilon_m = \varepsilon_m' + \varepsilon_m''$, and ε_d denotes the medium's dielectric constant, which is proportional to its refractive index with $\varepsilon_d = n_d^2$. This is the fundamental idea behind refractometric sensing technologies. The real component of ε_m must be negative and its absolute value must be less than ε_d for SPP excitation and propagation. Only materials having a dielectric constant with a large negative real component and a small imaginary part are required for dielectric permittivity requirements. This criterion is satisfied for a variety of metals at optical wavelengths, with gold, silver, and aluminum being the most often utilized in plasmonics [5]. Additionally, since these metals have a smaller imaginary component of their refractive index, they exhibit much reduced plasmonic reduction compared to other materials, resulting in decreased loss while propagating. Biochemical interactions along the metal-dielectric interface's vicinity cause RI changes, which affect the SP's propagation condition. Without the requirement for labeling, these changes may be followed in real-time, resulting in a meaningful signalization [6].

As demonstrated in Figure 1, the SPP's evanescent field is localized to the metal-dielectric interface and decreases exponentially in both media. When operating in the visible (VIS) and near-infrared (NIR) ranges, aymmetric field occurs with the majority of it concentrated in the dielectric close to the surface and a typical penetration depth of 100-500 nm [4], which is particularly notable for SPR sensing, as it uses SPPs in optical

sensing and acts as a the depth probe. This implies to biomolecular interactions on the metal layer and with the aid of evanescent field depth of penetration would generate measurable changes in the SP.

1.1.2 Surface Plasmon Resonance

The area of nanoplasmonics research is concerned with light-induced collective free electron oscillations between dielectrics and materials containing a lot of free or free-like electrons. Surface plasmon resonance refers to the phenomenon of electron collective oscillation (SPR). At the nanoscale level, the SPR enables light manipulation below the diffraction limit. The SPR resonance can be controlled by varying its geometric parameters as well as the dispersion properties of its constituent components. The dielectric layer's fast-decaying evanescent field becomes particularly sensitive to fluctuations in the environment's refractive index when incoming photons form surface plasmons at a metal-dielectric interface. A proximity-based approach may achieve high sensitivity and minimal detection constraints [4]. SPRs propagate as limited modes on flat metal/dielectric surfaces. On the metal-dielectric interface, a high refractive index prism or periodic gratings may be used to overcome the momentum matching requirement for photon coupling from the dielectric to the surface-confined mode. Only if, the component of the light's wave vector parallel to the contact matches the SPP propagation vector can the SPR be activated by connecting incident light to the surface plasmons;

$$k_x^{light} = \frac{2\pi}{\lambda}\sqrt{\varepsilon_d}\sin\theta \tag{1.3}$$

The above equation will be equal to k_x^{SPP} but SPs are not capable of stimulating by direct excitation because the SPP propagation vector is much bigger than the dielectric light wave's wavenumber. To improve the wave vector of the incident light; a prism coupling, a waveguide coupling, or a grating coupling may be used. The Kretschmann or Otto configurations, which use a prism to give the required momentum to activate SPR in a thin metal layer, are used in commercially available SPR sensors [7]. These sensors aren't molecule-specific and therefore need a complex experimental setup. Hole arrays enable the coupling prism to be removed, simplifying the sensor. LSPR and SPP, which have distinct refractive index sensitivities and effective sensing distances, are also supported

by nanohole arrays. For phase matching prism copuling based in Kretschmann configuration, equation (1.4) must be satisfied.

$$n_p \sin\theta - n_{spp} = 0 \tag{1.4}$$

where n_p is the coupling prism's refractive index and the angle of incidence is θ. The exceptional refractometric sensing of dispersive materials in the interface of the metal-dielectric interface is enabled by a direct relationship between the SPP wavevector and the media's local dielectric permittivity. The following expression shows the refractive index sensitivity (S_B) for grating-based coupling:

$$S_B = \frac{\frac{\partial n_{spp}}{\partial n}}{\left(\frac{m}{\Lambda} - \frac{dn_{spp}}{d\lambda}\right)} \tag{1.5}$$

where m is the order of diffraction, and Λ is the period of the grating. This refractive index sensitivity can be used in a biosensor environment if the thin film metal surface is biologically functionalized. The SPP evanescent field decay within the dielectric media is considered in this circumstance. SPP decay length is determined by the dielectric behavior of the constituent metals, dielectrics, excitation wavelength, and excitation geometry, and is typically between 150-400 nm perpendicular to the metal-dielectric interface. The change in local RI generated by the analyte can be attributed to the medium's refractive index. Surface sensitivity (S_S) term associated with the SPP-based biosensing can also be calculated:

$$S_S \sim S_B \exp\left(-\frac{2d}{l_d}\right)\left[-\exp\left(-\frac{2t}{l_d}\right)\right] \tag{1.6}$$

from formula the distance from the metal-dielectric media interface is *d*, the thickness of the layer is *t* where the RI change occurs. Figure of Merit ($FoM_{B/S}$) relationship can be employed to define performance of the sensor. For this purpose, the ratio of the refractive index sensitivity (S_B or S_S) and full-width half-maximum of the detection signal (w) should be calculated:

$$FoM_{B/S} = \frac{S_{B/S}}{w} \tag{1.7}$$

$$w \sim 4\gamma \frac{d\lambda_r}{dn_{spp}} \tag{1.8}$$

where radiative (γ_r) and absorptive attenuation (γ_a) coefficients are considered to be equivalent. The plasmonic material's resonant wavelength and permittivity can significantly affect the bulk RI sensitivity of Kretschman configuration-based SPR. Even though there is an exponential relationship between the RI sensitivity of bulk material and wavelength of resonance implying wavelength adaptable performance, with increasing resonant wavelength, the EM field decay constant increases exponentially. As a result, the generating surface RI sensitivity is considered useless for biosensing. SPR, on the other hand, compensates for its large l_d by having a high bulk sensitivity for biosensing. It is worth mentioning that, SPR method needs precise thermal stability because of its large l_d. In other words, even very small temperature changes can decrease the signal-to-noise ratio causing some crucial problems for SPR's adoption into portable devices.

1.1.3 Localized Surface Plasmons

For metallic nanoscale bodies, i.e., nanoparticles, the plasmons cannot propagate because there's nowhere for them to go. Therefore, they are entirely restricted to the object's surface. Since they are confined, there isn't any momentum and could be activated by incoming photons by coupling to electromagnetic radiation. These are called as localized surface plasmons (LSP) and stimulated at specific resonance frequencies that are typically in the visible range, allowing light to be localized below the diffraction limit as well as improved scattering and absorption of photons [8].

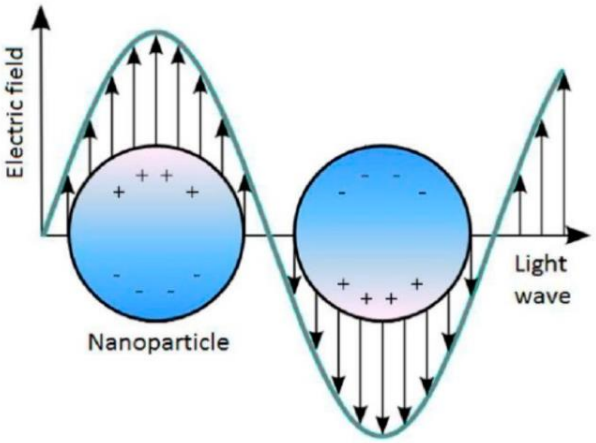

Figure 2 Schematic of localized surface plasmon for a metallic nanoparticle. An incoming electromagnetic field disturbs the free electrons, which are negatively charged, in the particle, leaving behind a positively charged particle. Oscillation starts at dipole resonance [9].

1.1.4 Localized Surface Plasmon Resonance

Metallic nanostructures with a wavelength less than the incoming light may sustain locally limited collective harmonic oscillations without propagating of free electrons in the interface of metal-dielectric. This method is an alternative to SPR. Localized surface plasmon resonance (LSPR) is used to describe this phenomenon. If the thin metal film's volume is decreased until its dimensions are less than the incoming wavelength, the electrons across the nanoparticle oscillate in phase. Localized surface plasmon resonance occurs on curved metallic surfaces, including metallic nanoparticles and voids of different topologies, with the topology providing the extra momentum to link directly to incoming light [10]. Electrostatics may be used to approximate the electromagnetic characteristics of LSPR. The metallic objects' form, size, and dielectric constant influence the boundary conditions that define the LSPR frequency [11]. LSPR allows for extremely concentrated incident light, so a strong local electromagnetic field is produced. This mechanism causes polarization charges to accumulate on a nanoparticle's surface, turning it into a dipole. The dipolar field and the EM field close to the nanoparticle surface is elevated due to improved light absorption and scattering.

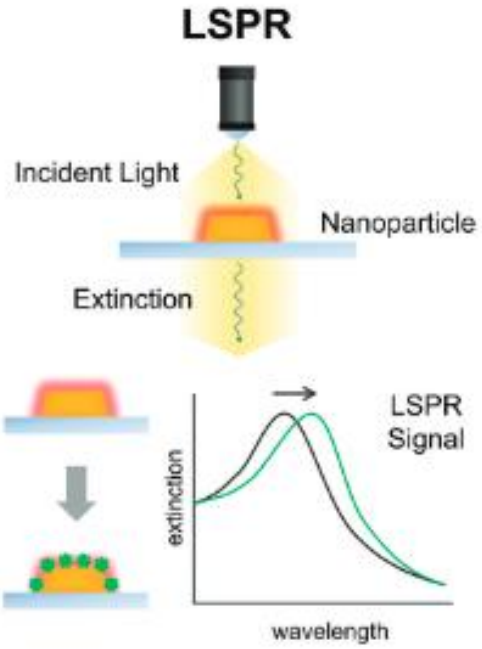

Figure 3 Schematic of measurement concept, nanostructure geometries, and spectrum information derived from nanoplasmonic sensors based on LSPR [12].

The source of LSPR is the excitement of collective oscillations of electrons in a metal nanostructure with a considerably smaller size than the wavelength of the incoming photons. Since the nanostructure layer is shorter than the decay length of propagating surface plasmons, plasmonic oscillations produce non-propagating waves. A modified version of Mie theory [13] can be used to describe the spectral extinction cross-section profile of metal nanostructures as follows:

$$\sigma(\omega) = \frac{18\pi V \varepsilon_d^{3/2}}{\lambda} \frac{\varepsilon''(\omega)}{(\varepsilon'(\omega) + \chi\varepsilon_d)^2 + (\varepsilon''(\omega))^2} \tag{1.9}$$

wavelength of the incident photon is described by λ, V is the volume of the metal nanostructure, ε_d is the permittivity of dielectric media frrom surrounding, real $\varepsilon'(\omega)$ and imaginary parts $\varepsilon''(\omega)$ of the permittivity, and χ is a modification parameter varying with the nanoparticle shape where $\chi = 2$ for a sphere.

Depending on the nanostructure geometry, the highly localized EM field decays quickly, resulting in an extremely short evanescent field decay length of roughly 10-50 nm. A shorter decay length improves the refractometric surface sensitivity of LSPR-based sensing devices. For identifying tiny molecules close to the metal-dielectric contact, it

provides a significant advantage over traditional SPR. The thickness of the target-specific biorecognition layer must be considered because of the short decay lengths in LSPR biosensing. The following equation can be used to express the surface sensitivity of an LSPR-based nanostructure;

$$S_S \sim S_B \exp\left(-\frac{2t_0}{l_d}\right)\left[1-\exp\left(-\frac{2d}{l_d}\right)\right] \tag{1.10}$$

where t_0 is the initial thickness of the biorecognition layer, and d is the distance away from the metal-dielectric interface. As a result, the figure of merit for surface sensitivity was also adjusted using the following equation with plasmonic response of w which is the spectral width;

$$FoM_s = \frac{S_s}{w} \sim \frac{S_B}{w}\exp\left(-\frac{2t_0}{l_d}\right)\left[1-\exp\left(-\frac{2d}{l_d}\right)\right] \tag{1.11}$$

1.1.5 Extraordinary Optical Transmission

The extraordinary optical transmission (EOT) deals with the increase in optical transmission through subwavelength apertures in a metallic film when surface plasmon polaritons (SPP) are excited. Periodic arrays of nanoholes are widely used for the EOT sensing schemes. The hole array in a patterned metal film provides the additional velocity required to excite an SPP directly. Furthermore, through the nanohole array, the SPP on the incident light side can couple or transfer to the opposite side of the metal film, because of the increased momentum provided by the hole array. The SPP can then re-radiate into the far-field, the subwavelength SPP mode couples through the metal layer and subsequently radiates again, this allows for a higher light transmission through the metal nanohole.

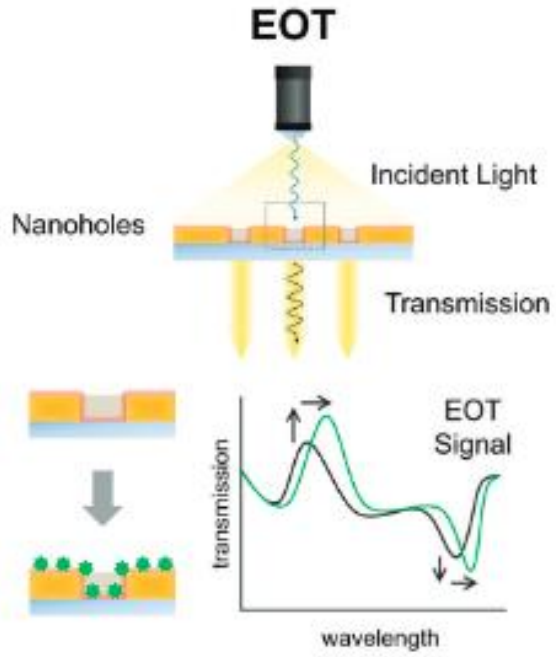

Figure 4 Schematic of measurement concept, nanostructure geometries, and spectrum information derived from nanoplasmonic sensors based on EOT phenomena [12].

Extraordinary optical transmission (EOT) phenomenon was suggested through subwavelength nanohole arrays [14]. The study showed that zero-order transmission was possible in 2D nanohole arrays on silver thin films at wavelengths ten times larger than the nanohole diameter. Unexpectedly, the set of peaks got stronger at longer wavelengths, even when the periodicity a_0 minimum was reached. A second minimum was found at $\lambda = a_0\sqrt{\varepsilon_s}$, related to the interface of metal–quartz and the substrate's dielectric permittivity ε_s. Diffraction from the array and individual nanoholes was also absent for $\lambda > a_0\sqrt{\varepsilon}$. The periodicity of the array determines the transmission maxima. The full-width half-maximum of the transmission peaks is highly influenced by the cylindrical holes' depth/diameter aspect ratio. SPP can tunnel through the holes that act as a waveguide as it propagates through the metal-dielectric interface, causing EOT. When the aspect ratio is 1, the sharpness is at its highest point [15]. The hole array works as a diffraction grating, providing the extra momentum needed to couple incident light to the SPP mode. As a result, the excited SPP can scatter back into the far field when it passes through the subwavelength apertures on the metallic sheet. The light is re-radiated through contrary side of the film from the incident light if the SPP tunnels through the sub-wavelength apertures or couples to the opposite side of the film. This results in a

higher transmission. When the incident photons momentum and the grating's momentum matched, SPs get activated, as stated by equation 1.12;

$$k_{sp} = k_x \pm nG_x \pm mG_y \tag{1.12}$$

where k_{sp} is the surface plasmon wavevector, $k_x = \left(\frac{2\pi}{\lambda}\right) sin\theta$ is the element of the incoming light's wavevector within the grating's plane and $G_x = G_y = 2\pi/a_0$ are the grating momentum wave vectors for a square nanohole array [15]. In the first approximation, the equation below specifies the dispersion relation of the resonant peaks associated for EOT in periodic arrays in metal sheets:

$$\lambda_{EOT} \cong \frac{\Lambda}{\sqrt{i^2 + j^2}} \sqrt{\frac{\varepsilon_d \varepsilon_m}{\varepsilon_d + \varepsilon_m}} \tag{1.13}$$

where Λ represents the period, i and j are integers representing diffraction orders. These dispersion relations, which relate to the wavelengths of the resonant modes of SPPs, close to the resonance wavelength of plasmonic nanohole arrays, allowing them to be controlled by changing the nanoholes' period. [16].

$$S_B = \frac{\frac{\partial n_{spp}}{\partial n}}{\left(\frac{\sqrt{i^2+j^2}}{\Lambda} - \frac{dn_{spp}}{d\lambda}\right)} \tag{1.14}$$

The sensitivity of EOT-based sensing adjusted with the wavelength of the resonance. The period of the nanohole array may be changed to change the resonance wavelength. In the spectrum response of a nanohole array, higher diffraction orders will introduce extra transmission peaks. EOT's refractive index sensitivity will be lower than SPR's because the ratio of diffraction mode number and period adds to the denominator of the sensitivity term. In the case of SPR, the term $\partial n_p/\partial \lambda_r$ is negligibly small and denominator is defined by $\partial n_{spp}/\partial \lambda$. Meanwhile, $\sqrt{i^2 + j^2}/\Lambda$ term will diminish the effects of material related $\partial n_{spp}/\partial \lambda_r$ term. In comparison to the significantly lower S_B of widely used nanodisks, EOT offers a higher level of S_B. EOT-based biosensing, unlike LSPR, does not require polarized light sources to activate SPPs. Despite the fact that EOT is an SPP-based phenomenon, the evanescent field decay length is comparable to LSPR and much shorter

than conventional SPR. The EM field augmentation appears at the edges of nanohole, resulting in greater field confinement than SPR.

For larger analytes as viruses, cells, and bacteria, EOT has a better detection geometry than LSPR. Sensing performance can be improved with SPR-based sensing, at least theoretically. Due to the shorter decay lengths of plasmons in EOT and LSPR sensing, they can be more compact and portable, have more surface sensitivities based on analyte type and concentration, as well as low temperature sensitivity [4].

1.2 Plasmonic Materials

Metals can be used to create a plasmonic device. Plasmonics is the study of light's interaction with metals or metallic nanostructures. They have many free electrons activated by an electromagnetic wave, creating collective oscillations. This activation is the plasmon phenomena that optical devices' working principle. Plasmonics combines several techniques at nanometer size to conduct optical evaluation of spectra and refractive index alterations linked to chemical structure or binding events. It can support the extraction of useful data about the concentration, or identity of molecules in the fields of photonics and electronics. The dielectric function, $\varepsilon(\omega)$, may characterize plasmonic materials in terms of the optical responses, and the angular frequency of the light is ω. The dielectric function's real part of plasmonic materials is negative. Every plasmonic material must be capable of creating a negative real permittivity to be used in a plasmonic device. Since metal has free electrons, it is often used as a plasmonic material [17]. The dielectric function of metallic materials can be defined by the Drude model:

$$\varepsilon_{Drude} = 1 - \frac{\omega_p^2}{\omega^2 + i\gamma\omega} \tag{1.15}$$

where γ is the bulk electron collision frequency, i is the imaginary unit, and ω_p is the free electrons' bulk plasma frequency. This signifies that the incident light will have an effect on the material's optical characteristics [18]. When a metallic nanoparticle interacts with incoming light, the local photonic density of states in the vicinity of the structures

increases, changing the optical properties of nearby molecules, like their impulsive emission rate. As a result, these interactions may be used to effectively increase and modify light interaction, allowing for a variety of biosensing applications [19].

On the other hand, metals lose much of energy due to interband electronic transition in the Visible and Ultra-Violet frequencies [20]. There are two forms of losses in metals, each reflecting a different type of interaction. Firstly, ohmic loss, which indicates the flowing electrons resistance as defined by the carrier mobility. Carrier mobility must be high for plasmonics. Secondly optical loss, which results from electronic transit resulting in intra- and inter-band losses, these should be lower. Additionally, the carrier concentration is another material parameter critical for material optimization since it dictates the wavelength range across which the material is activated. High carrier concentrations in metals produce visible and ultraviolet responses, whereas low carrier concentrations in semiconductor materials produce infrared to THz responses. Metals suffer optical losses at optical frequencies due to interband and intraband transitions. The free electrons travel from an occupied state to unoccupied one results in optical losses in metals. Silver, copper, and gold have comparatively low ohmic losses due to their great electrical conductivity. While most metals have low ohmic losses and excellent electrical conductivities. Thus, the optical loss remains an issue. Silver and gold have the highest electrical conductivity, but it is a significant barrier to their development in plasmonic devices. As a consequence of these losses, the performance of plasmonic devices is damaged, and their applications are limited [21].

Silver (Ag) has the lowest loss at optical frequencies compared to other metals, making it the best choice for plasmonic devices. Although gold (Au) has a more considerable loss than silver at about 500 nm, it is primarily used as a plasmonic material in the lower NIR region due to its chemical stability [17]. Another metal used as a plasmonic material is copper (Cu), which has higher losses than silver and gold at most optical wavelengths. One of the uses of plasmonic devices is LSPR sensors, with gold being the preferred plasmonic material due to its chemical stability [22]. Several metals with higher optical losses than gold and silver, such as platinum (Pt) and palladium (Pd), have been used as plasmonic materials where functionality affects overall device performances [23]. Other metals such as aluminum (Al) and magnesium (Mg) have been investigated to solve this device application problem. They show plasmonic resonances in the UV range, but they

are unsuitable for biosensing since biological organisms absorb UV light and physically decay [24], [25]. One of the primary criteria determining the frequency of plasmonic resonance is the charge carrier density number. As a result, the flexibility to modify the number of charge carrier densities while building a plasmonic device is helpful. This parameter is fixed in metals. Hence the optical parameters aren't adjustable [26]. Consequently, geometrical changes restrict the control of metals' plasmonic response, lowering design variety dramatically. New materials are needed because of the disadvantages of metals in plasmonic applications.

1.2.1 Transition Metal Nitrides

In the visible and longer wavelengths, metal nitrides such as titanium nitride, zirconium nitride, tantalum nitride, and hafnium nitride display metallic characteristics. These are interstitial compounds with high free-carrier concentrations that are non-stoichiometric. Transition metals (TMN) are excellent optical conductors because their d and p orbitals are partly filled and overlapped [4]. These materials are also refractory, stable, and hard, and their optical characteristics may be tailored by changing their composition. Transition metal nitrides, such as titanium nitride (TiN), are non-stoichiometric ceramic materials. In other words, the composition, and the optical characteristics, are highly dependent on the technique and circumstances of synthesis [27]. The refractory nature of the TMNs is favorable since it avoids diffusion limits and shapes degradation over time. With their high melting point, chemical stability, and tunable charge carrier density, conductive ceramics are the best candidates to fill the gaps left by metals.

1.2.2 Titanium Nitride

Titanium nitride is a transition-metal compound that exhibits the properties of a refractory ceramic with covalent TiN bonding, a high melting temperature (up to 3000 °C), metallic properties showing golden color, and high electric conductivity. In terms of optical characteristics, TiN has recently been demonstrated to be a plasmonic material in both the visible and infrared (IR) spectrum ranges. Attention towards titanium nitride is growing rapidly because of its cost, strong electron conductivity, and mobility, its high

melting point, and it can overcome most of the disadvantages of plasmonic metals [28], [29].

TiN is a transition metal from group 4B in the periodic table. It contains four valence electrons in the $3d^2 4s^2$ structure. TiN's 3d and 4s energy bands overlap since the atomic orbitals of 4s are away from the 3d atomic orbital, which causes to have higher overlaping energy. Ti and N atoms form bonds in the configuration of $2s^2\ 2p^3$. Some of the nitride phases such as Ti_2N and Ti_3N_4 have been observed and concluded that the cubic rocksalt B1-TiN structure, δ-TiN, contains the most stable nitrides of these metals [30]. Electronic conductivity is caused by the partially filled valence Ti-3d orbitals that are not fully hybridized with the N-2p electrons leading to increased metal-like behaviour. B1-TiN optical characteristics that are important to plasmonic applications.

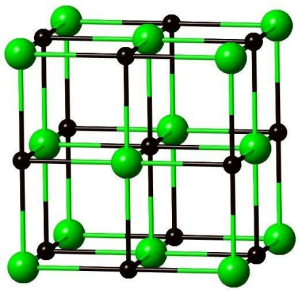

Figure 5 Cubic (rock salt) structure of B1-TiN [31].

1.3 Nanohole Array Fabrication Methods

The nanofabrication has proven to be a difficulty and a solution for PoC commercialization of plasmonic biosensors. To fulfill clinical application standards and replace traditional techniques, significant obstacles must be solved, like scalability, multiplexing, and biocompatibility. High resolution, defectless, and low cost, nanostructure production are requirements for effective nanofabrication. A wide range of manufacturing methods ranging from nanoparticle synthesis to advanced lithography have been reported in the literature. In large area array fabrication, nanosphere lithography (NSL), nanoimprint lithography (NIL), electron-beam lithography (EBL),

focused-ion beam lithography (FIB), and laser interference lithography (LIL) can be utilized instead of typical approaches like photolithography (PL). A comparison of these methods will be discussed.

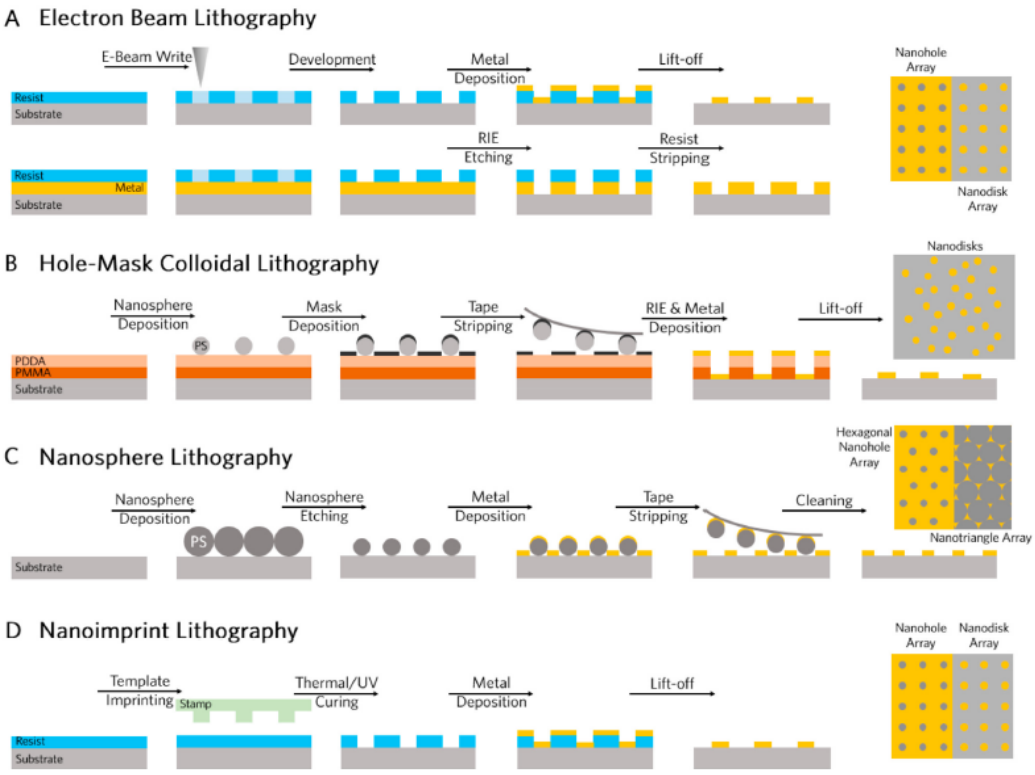

Figure 6 Nanofabrication methods that are often employed in nanoplasmonic biosensor applications [4].

Photolithography (PL) uses light to transfer shapes from a photomask to the surface. It is originated from greek, where photo means light, litho means stone, and graphy, writing. Photolithography is used to generate particular patterns in a material, is one of the most essential and simple microfabrication processes. A form or pattern can be etched using this approach by selectively exposing a light-sensitive polymer to UV light. There are numerous limitations of photolithography. Some of them can be listed as unsuitable for curved surfaces, diffraction restricted, photosensitive polymers are required, masks are pricey, and due to the rigorous processing conditions, it cannot be employed in biological samples [32].

Electron beam lithography (EBL) is a well-established lithography technique for the precise fabrication of features smaller than 100 nm [33]. EBL can be used to translate a bespoke design with nanoscale accuracy onto a flat with e-beam(electron-beam) sensitive resist coated surface by a focused electron beam. After the electron beam exposure, the sample could be passed to further production stages like metal deposition and lift-off processes [34]. For EBL, collimated beam diameter is in the angstrom region, resulting in very high resolution. Generally, EBL is used to manufacture LSP and nanohole array-based sensors. However, the lift-off process may cause challenges in achieving sharp edged structures once material has been deposited on the patterned substrate. These problems develop due to sidewall creation and electron beam dosage, which results in wavy pictures [34], [35]. The wavy sidewalls lead the EM to attenuate, causing it to wave quicker and decreasing the LSP resonance. Because of the low productivity and high cost in EBL, it has been limited to the generation of nanoscale patterns in very constrained regions.

Nanoscale designs can also be created using FIB, which provides resist-free structures comparable to EBL. The ion source type, scanning technique, beam characteristics, together with processing parameters affect the minimum feature size. Nanohole arrays on metal films were created using FIB milling [36]. The FIB method uses low accelaration ions to detach material from a sample by collision and can achieve 10 nm resolutions [37], [38]. Gallium is the utmost used source metal ion in FIB milling. However, Au–Si–Be and other alloys also might be utilized. FIB milling is a direct-writing process that allows precise tuning of ion invasion depth by altering ion energy. However, similar to EBL, this method is unlucrative. It takes longer time, and restricts mass manufacturing of nanohole array-based sensors.

Another approach is laser interference lithography (LIL) as a technique for fabricating nanohole arrays in metal sheets that is efficient, versatile, and scalable. It is a technology that involves the maskless exposure of a photoresist layer with two or more coherent laser beams. A coherent UV laser is cleaned and expanded using a optical filter. Perpendicular to each other, a mirror, and an inclined resist-coated substrate are constructed. The extended laser beam impacts an oblique mirror and a slanted polymer resists–coated substrate at the same time. The mirror's reflection is also incident upon the surface. On the substrate, incoming and reflected light collide, forming a standing wave pattern. The

infamous Lloyd's mirror interferometer is the basic configuration [39]. While laser interference lithography is a significantly quicker and less expensive approach for maskless parallel patterning, it falls short of EBL regarding pattern consistency and pattern flexibility. These limitations of LIL may be attributed to need for high precision optical processing [40].

NIL utilizes the notion of mechanical modification of a thin polymer film in a thermo-mechanical or UV curing process utilizing a template/mold holding the micro/nanopattern. It employs hard contact between the mold and the thermoplastic to imprint the pattern, rather than expensive and sophisticated optics and light sources. Template manufacturing, overlay alignment, defect control, high yield, and finding particularly relevant application domains are now critical problems for NIL. Before NIL can be used in semiconductor production, it must overcome two major obstacles: alignment and template/mold manufacture [41].

Nanosphere lithography (NSL) is a low-cost, scalable, and repeatable fabrication technique that uses a self-assembled monolayer of polystyrene nanospheres (PSNSs) on a substrate surface to form a mask and then evaporation or etching processes for fabrication. Combining NSL and e-beam deposition allows for the fabrication of large-area NH arrays. Metal vapor condenses into the pores of the pre-etched PSNS monolayer during deposition, producing NH structures [42]. Also, it is known as colloidal lithography. Surface patterns with great accuracy and consistency across wide regions are created using colloidal monolayers as templates. A colloidal layer is pre-assembled on a substrate and employed as a shadow mask during the material deposition process. After the colloidal particles are removed, defined surface nanostructures with a high degree of order and hexagonal symmetry are created, inherited from the colloidal templates. NSL lacks the perfect order that LIL can attain, but it does have the benefits of adaptability and experiment simplicity. Commercially accessible spherical colloids of silica and polystyrene with sizes ranging from 100 nm to microns may also be made using well-established techniques. Their self-ordering, based on Langmuir–Blodgett processes, involves basic laboratory glassware and a syringe pump [43]. The particles near the liquid interface are mechanically squeezed by barriers, resulting in a densely packed monolayer.

1.4 Nanoplasmonic Biosensor

According to the World Health Organizations' prediction of escalation in chronic and infectious diseases, healthcare workers needed fast action to diagnose and improve treatment procedures for patients to have a healthy and comfortable life. With the rapid increase in diseases, nanotechnology has emerged to uncover disease-related biomarkers with simple, cost-effective, and portable solutions. To sustain fast, sensitive, label-free, and real-time measurements, point-of-care testing (POCT) enables personalized treatment and is advantageous for widening approachability by being in the site of the patient. POCT devices involve biosensors, smartphone (SP)-based technologies, microfluidics, paper-based sensors, lab-on-a-chip (LOC)-based, and multiplex immunoassay types [44].

There has been a compelling improvement in nanobiotechnology, and biosensor need have increased. The market of biosensors was valued at 25.5 billion USD in 2021 and it is anticipated to reach 36.7 billion USD in 2026. Minituarized devices provide new possibilities to construct tiny and handheld systems that may help globalize clinical analysis or even be embedded within the organism. The use of biosensors is becoming increasingly common in many areas to determine the quality of the field of interest, such as changes in physiological processes. Biosensing has been a useful technology in recent decades due to the label-free detection of biomolecules and complex structures, and real-time detection of biomolecules and complex structures have been achieved [45]. Both the bioreceptor and the transducer are essential components of a biosensor since they are responsible for converting the recognition event into a signal that can be analyzed [46]. Biosensors are divided into categories depending on their transducer types; mass-based, electrochemical-based, and optical-based. They are also classified according to their detection method whether label-free or label-based [47], [48]. A label is defined as any foreign molecule that is chemically or temporally linked to the molecule of interest to detect the existence or activity of the molecule of interest, and which can affect the intrinsic features of the molecule of interest [49]. A label-free method is a detection for non-labeled target molecules or the screening of analytes that are difficult to tag. It removes the necessity for these particular labeling techniques involving markers and dyes, providing more selective detection of the target analyte [50]. A new strategy is

necessary for rapid and sensitive results due to the consumption of time, workload, and multistep analyses that demand well-equipped labs. Bionanotechnology and nanofabrication advancements have resulted in considerable improvements in resolution, detection sensitivity, and multiplexing. Nanoarray technology allows for high-throughput screening with pinpoint accuracy. It is frequently used in labs to investigate and characterize the underlying causes of various diseases and develop novel therapeutic medications [51]–[53]. There is an increasing need for more comprehensive and cheaper healthcare procedures that allow for localized analyses, specifically the generation of accurate point-of-care devices [54].

Devices used at the side of patients are tiny, portable, and easy to use equipment that can react fast, sensitively, and accurately to a wide range of biomarkers using minor sample amounts. PoC devices are often developed either as lateral-flow tests or biosensors [55]. Biosensor devices with small sample quantities and little preprocessing may deliver accurate quantitative analytical information in seconds. A biosensor uses a biological recognition element in close contact to provide extremely quantitative analytical information with transducer [56]. Biological data is sensed when a transducer detects a series of physicochemical changes in the liquid or on the interface.

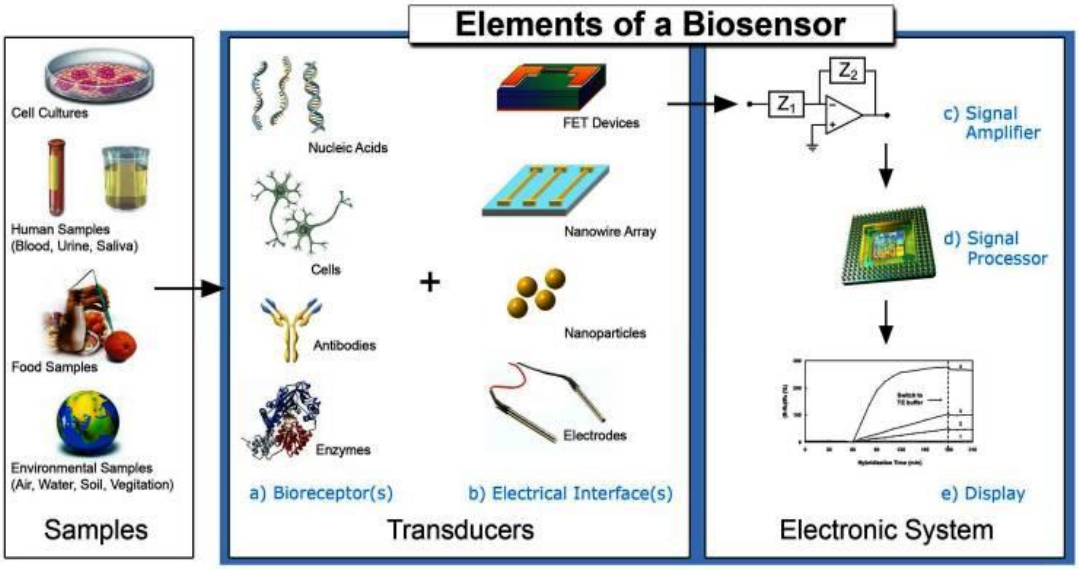

Figure 7 Elements of Biosensors [57].

The concept of an optical biosensor is to create signals proportionate to the analyte's concentration and allows label-free and real-time parallel detection. Transduction alters the absorption, transmission, reflection, refraction, phase, amplitude, frequency, or polarization of light in response to physical or chemical changes caused by biorecognition elements [58]. There are several types of optical sensors. Electromagnetic (EM) waves can be restricted in a variety of dielectrics or metals, resulting in either a localized or propagating manner of detection. When a component of the EM wave is absorbed by the external medium, an evanescent field is created. The evanescent field is employed as a probe that does not require a label to detect refractive index (RI) shift, such as those generated by biological interactions. Plasmonic biosensors are an example of an evanescent wave biosensor [59], [60]. These devices have a number of advantages, including high detection sensitivity, quick response times, immunity to electromagnetic and mechanical interference, and the ability to be downsized. Plasmonic biosensors offer an advantage over other optical biosensors in that binding events are not revealed by labeling the analyte with an optically active marker. Plasmonic biosensors are label-free detecting devices with high sensitivity and specificity for monitoring biomolecular interactions in real time. Plasmonics has been widely used in biosensing with improved sensitivity for refractive index (RI) alterations and increased light-matter interactions because of its capacity to produce nanoscale hot spots that are near the size of bioparticles [61].

2 MATERIALS & METHODS

2.1 Materials

All chemicals, including acetone, ethanol, methanol, sodium dodecyl sulfate (SDS), ammonia solution (25%) were bought from Sigma-Aldrich, USA. Deionized (D.I.) water produced by the Milli-Q Integral 3/5/10/15 system (18.2 MΩ·cm, Millipore Corp., USA). Substrate microscope slides made out of soda-lime glass (SLG) were purchased from Thermo Fisher Scientific, USA. Silicon wafers (100) were bought from Siegert Wafer GmbH, Germany. The cleaning concentrate Hellmanex™ III is from Sigma-Aldrich, USA. Polybead® Polystyrene 0.35, 0.5 µm microspheres were from Polysciences, Inc., USA. The components used for sputtering and evaporation; targets and tungsten boats were supplied from Kurt J.Lesker, Germany.

2.2 Methods & Equipments

2.2.1 Substrate Preparation

The substrates were cleaned before use in two states to obtain surfaces without any impurities and have high-density, close-packed particles. As substrates, silicon and soda-lime glass (SLG) was used. The first treatment is using Hellmanex® III alkaline solution, which is highly effective in cleaning glass surfaces for optical purposes. The substrates were put in chalet horizontally in 2% concentration of Hellmanex solution for 1 hour at the temperature of 50°C. Since it is an alkaline liquid rich in organic active cleaning

agents, it reduces surface tension and increases the wettability of surfaces to avoid nanoparticles sliding around. After an hour, glasses were rinsed off with Milli-Q water and ethanol, respectively. The second treatment uses oxygen plasma to remove any organic and inorganic matter like contaminants and water vapor. By introducing oxygen gas into the system for 20 minutes high-frequency plasma will remove any residue left behind. This process will increase the hydrophilicity and bonding ability and surface modification.

2.2.2 Self-Assembled Monolayer of Polystyrene Nanospheres

The diameter of 500 nm polystyrene (PS) nanospheres is used. While substrates were in cleaning process the colloidal suspension of polystyrene nanospheres are prepared by mixing nanospheres (250µl) and ethanol (250µl) in an eppendorf tube and left in sonicator to disperse well for an hour before use, to avoid any aggregation of particles. After cleaning and mixing, the system for the experiment is set. The two dimensional (2D) array of colloidal crystals will be formed in a simple and rapid fabrication method at the water/air interface. The floating mechanism of the monolayer is formed with the aid of sodium dodecyl sulfate (SDS) and ammonia solution (25%). The water phase is prepared with 0.1 mM SDS solution and 20 mL of ammonia solution. The pH of the media is adjusted to 11.4. The surfactant, SDS, molecules move towards the surface of the water and forces particles to be closely packed together, creating ordered 2D hexagonal structure [62]. Since every batch is different from each other, the speed of the syringe pump is arranged according to the flow of nanospheres.

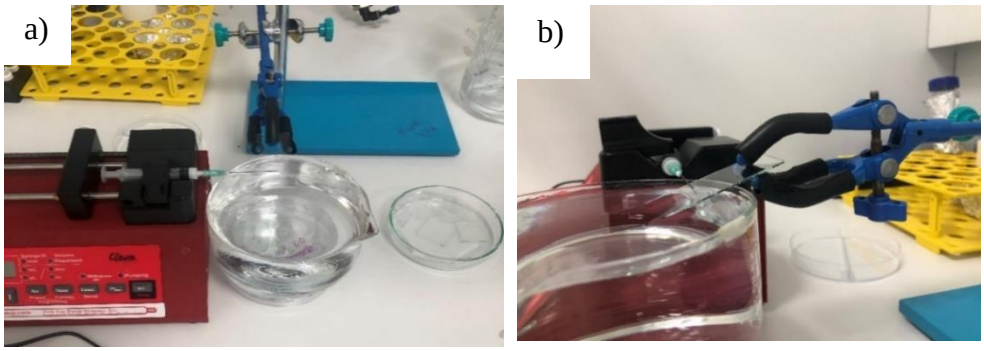

Figure 8 The setup for self-assembled monolayer formed with the aid of syringe pump. a) top-view, and b) side-view of the setup.

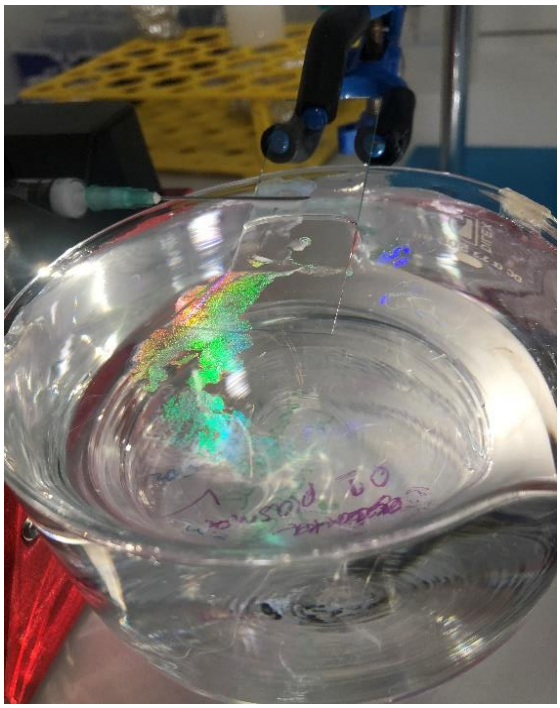

Figure 9 Monolayer of nanospheres growing on the air/liquid interface.

After the formation of the monolayer, they are collected with the glass substrates. By holding the substrates with tweezer, they are slowly dipped into the water phase. The monolayer is centered onto the substrate and collected by pulling it out holding in a flat position. Then, samples are left to dry at room temperature. While the solvent starts to evaporate, the capillary force pushes nanospheres to each other and forms a hexagonal stacked array. Figure 10 shows the images of PS nanospheres of 500 nm diameter taken with SEM.

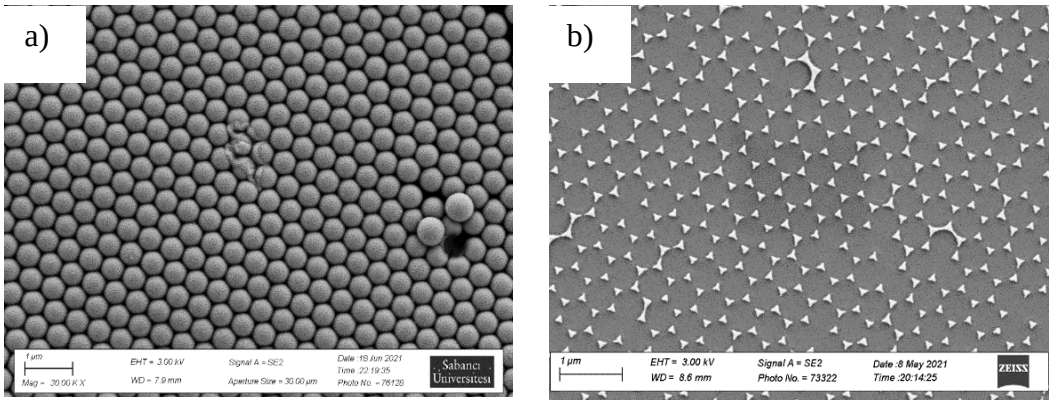

Figure 10 a) Self-assembled nanospheres. b) Remaining pattern after the deposition of metal and lift-off of nanospheres.

2.2.3 Colloidal Lithography

There are several nanolithography techniques. Colloidal lithography (CL) is founded on the concept of short-range order, which refers to the positioning of atoms in a predictable organized short distance with a small number of voids [54]. With the works of Deckman and Dunsmuir in 1982; Hulteen and Van Duyne in 1995 [64], micro and nanospheres may be employed as components of self-assembled masks for large-area nanofabrication of surfaces and thin films. Colloidal lithography is a rapid and straightforward process for producing nanoholes and nanodisks on surfaces. Colloidal lithography provides the foundation for subsequent procedures like thin film deposition, reactive ion etching, and epitaxial growth. Polymer colloids are heterogeneous dispersions of polymer spheres of variable diameters in aqueous or nonaqueous liquids for self-assembly. Polystyrene nanospheres are employed in experiments due to their widespread usage in optical, electrical, and photonic applications and their surface properties, tunable properties, and orderly structures seen in nature [65]. Self-assembled building blocks place onto surfaces in a dense periodical array structure. Both strong and weak forces act on nanospheres to be packed closely to each other; some examples are ionic, capillary, and hydrophobic. The colloidal lithography method in experiments was based on an air-liquid interface, which requires spreading agents (ethanol), pH control, and surfactant (SDS) for packing. An illustration of the air-liquid interface is shown in Figure 11.

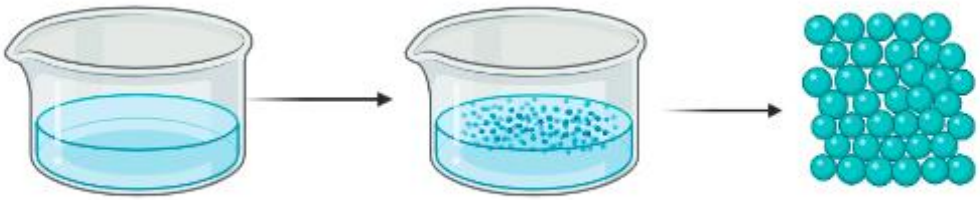

Figure 11 Schematic of PS monolayer formation at the air-liquid interface.

2.2.4 Syringe Pump

A syringe pump is a straightforward and convenient device that enables progressive immersion of liquids at a predetermined pace. After removing any surplus air from the

syringe's tip, a needle is attached to the device's handle part. The volume is specified in advance for the device based on the syringe's size. It is pushed from behind to drop or spin the liquid to provide a continuous flow of coating onto the substrate. It has been employed at the air-water interface to drop polystyrene beads into ammonia solutions and collect compressed bead islands, as depicted in Figure 11. The pace was determined according to the flow, which varied with each batch. The syringe pump utilized is a New Era Pump Systems NE-1000 programmable single syringe pump.

Figure 12 Syringe Pump NE-1000.

2.2.5 UV Ozone Cleaner

UV ozone cleaner is another simple, fast, and inexpensive method to have clean surfaces without any contaminations. The working mechanism is based on a UV light source with two distinct wavelengths, one at 185 nm and the other 254 nm, to break down organic residues. At these wavelenghts atomic oxygen is formed when molecular oxygen is detached with 185 nm and 254 nm ozone [66]. When both are present, atomic oxygen forms non-stop, and ozone is built and destroyed frequently to burn residues, leaving cleaned surfaces. The model used is ProCleaner™ by BioForce Nanosciences.

Figure 13 UV-Ozone Cleaner ProCleaner™ .

2.2.6 Plasma Treatment Systems

Plasma treatment systems are generally used to improve surface properties or cleaning processes. Plasma is generated in a vacuum environment by exciting a gas which can be argon, oxygen, nitrogen, or carbon dioxide with electrical energy [67]. If the gas reaches the optimum state by ionization, it will be called the fourth condition of matter, plasma. As a result, plasma produces charged particles and gets conductive and reactive, which helps modify the surfaces by making them easy to adhere to and more wettable. During the project, oxygen plasma is preferred to clean and activate surfaces of substrates. The processing variables of the system are pressure, plasma power, and gas. Throughout the project, high power is applied to glass surfaces for 20 minutes to increase the energy of surfaces and clean all the left residues. A plasma cleaner PlasmaFlo PDC-FMG by Harrick Plasma is used during the experiments.

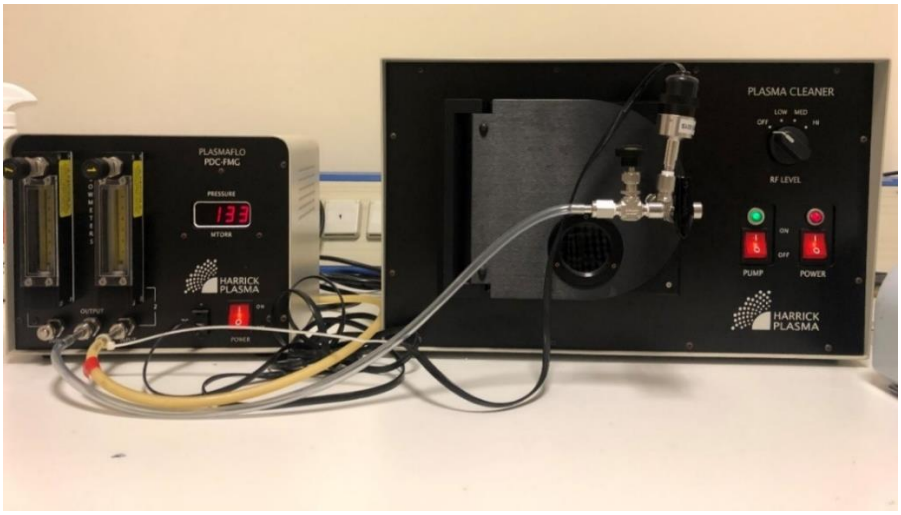

Figure 14 Harrick Plasma Oxygen Plasma Cleaner.

2.2.7 Plasma Asher

Plasma ashing is the process of removing polymer, volatile inorganic compounds, water vapor, or any non-metallic material from the surfaces by exciting plasma with oxygen gas in the vacuum chamber. Pressure is an essential parameter in this system. The pressure should be low to generate ionized gas with radio frequency, further producing plasma. In this project, it is used to remove polystyrene beads turning them to ash and pumped out with the vacuum to create a patterned surface behind. The optimization of the ashing process was studied with various power and time. The instrument used is from Torr International Inc., model R301.

Figure 15 Torr International Oxygen Plasma Asher-R301.

2.2.8 Physical Vapor Deposition

Physical vapor deposition (PVD) occurs under a high vacuum in a chamber that produces thin films and coatings by transferring material at the atomic level on a substrate [68]. A vacuum environment is advantageous in thin film deposition. For PVD deposition, the typical chamber pressure is on the order of 10^{-6} Torr. The high vacuum will remove air

molecules that are impurities to the deposited film. Also, a low vacuum environment is needed to sustain the plasma, and the mean free path of the particles will increase. PVD produces non-uniform, discontinuous films when conducted under an inadequate vacuum. Film quality is affected by different variables; evaporation rate, source-to-sample distance, and substrate shape. Substrate geometry is crucial in depositions when the substrate has a three-dimensional shape to prevent "shadowing", because the material is often deposited in a single direction, the first parts of the substrate reached by the evaporated material block other regions of the substrate and inhibit coverage, resulting in a shadowing effect. By use of a revolving stage lead to reducing this effect. Two instruments used the physical vapor deposition method in this project; sputtering and evaporation. Both methods turn source materials to a vapor phase from a condensed phase and adhere to the substrate as a thin film.

2.2.9 Evaporation Method

There are two coating ways; electron beam and thermal evaporation. Thermal evaporation evaporates the target material from solid to liquid, and then gas forms. The gas atoms disperse through the chamber and hit the substrate at the top of the chamber. The gas form of the materials solidifies when met with a cooler surface. Thermal evaporation is commonly used for metals like; gold, chromium, aluminum. The source is placed in a container called boat, clamped between electrodes, and heated from the sides with electrical current. The source melts and evaporates, traveling in the chamber until it coincides with a surface. The thickness of the film is monitored from the crystal sensor part of the device. If it reaches desired thickness, the shutter is closed which blocks evaporated particles to reach the sample, and the heating of the target is stopped, and the evacuation process of the chamber starts. Thermal evaporation is analogous to electron beam evaporation. The electron beam is created utilizing magnetic and electric forces by an electron beam. Magnets focus a filament, the electron beam, onto the source crucible. The source material atoms are heated to the point where they have enough energy to leave the surface and begin to evaporate. With a particular current, the concentrated beam of electrons may be changed. Depending on the material, high power might be required. The mechanism of deposition is identical to that of the thermal approach. Various targets can

be coated consequently. The device used is from Torr International, Figure 16. The working mechanism of both methods are illustrated Figure 17 and Figure 18, respectively.

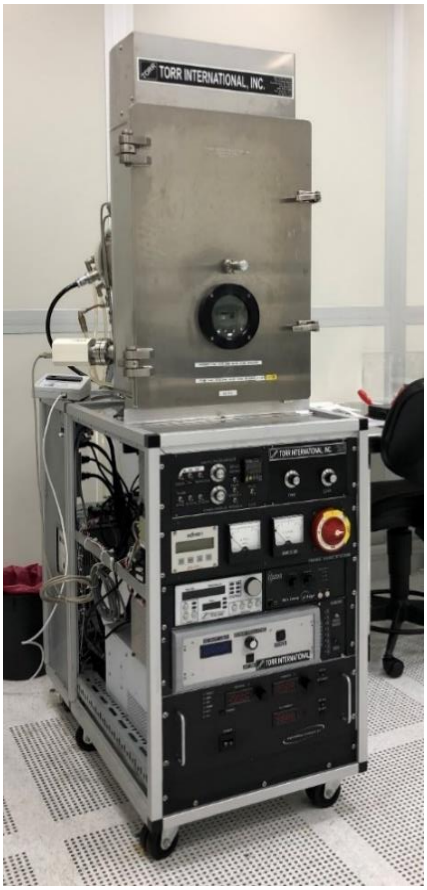

Figure 16 Torr International Evaporator.

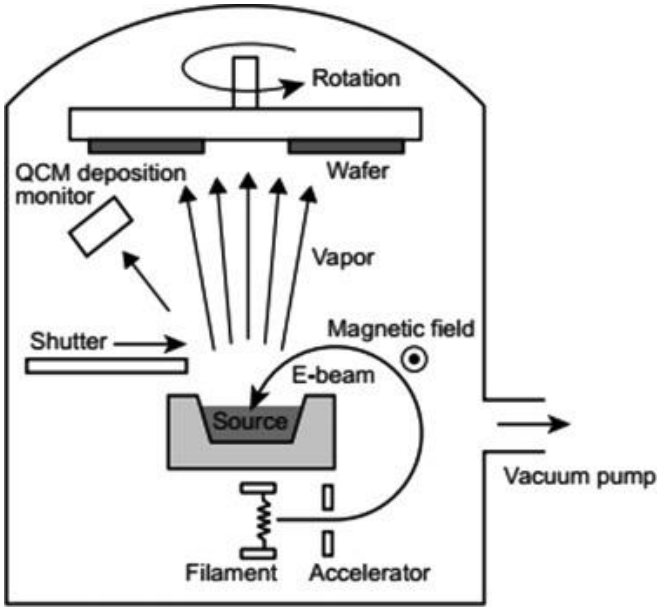

Figure 17 Schematic of electron beam evaporation [69].

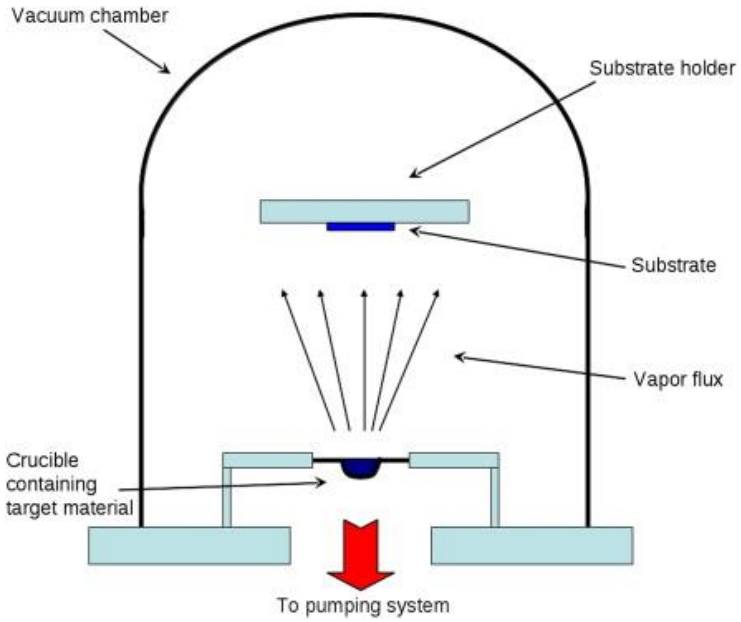

Figure 18 Schematic of thermal evaporation method [70].

2.2.10 Sputtering Method

Sputtering is another technique operating under a high vacuum medium, between 10^{-6}-10^{-7} Torr. The sputtering method used is called reactive magnetron sputtering. Reactive gases, also known as inert gases, are introduced into the chamber like Ar, O_2, N_2. Magnetrons increase the deposition rate placed behind the cathodes by elevating the number of electrons in the ionization for stable plasma. The target acts as a cathode, metal in a round shape, flat plate around 10-centimeter diameter is bombarded with high energy ions. The substrate and side of the chamber act as an anode. The energetic ions release target atoms upon impact to the surface and hit the sample surface directed by the magnetic field. The sputtered vapor of the metal condenses on the sample surfaces, and reaction with gas or gases are given into the system generates aimed film composition, for instance; nitrides, oxides [71]. The sample is rotating at the top of the chamber for a homogeneous distribution of the sputtered ions. Magnetrons highly increase the mean free path, yield, and growth rate by magnetically assisting the metal vapor. There are two source powers in the sputter chamber: radio frequency (RF) magnetron and direct current (DC) magnetron. The usage of the magnetron sources depends on the source material.

For example, for conductive or semiconductive materials, DC is preferred. For insulators and all conductors RF power, alternating current (AC) can be used because insulators require higher voltages to ignite. The sputter used is from Nanovak® NVSP-400, Figure 19. The working mechanism is illustrated in Figure 20.

Figure 19 Nanovak® Sputter NVSP-400**.**

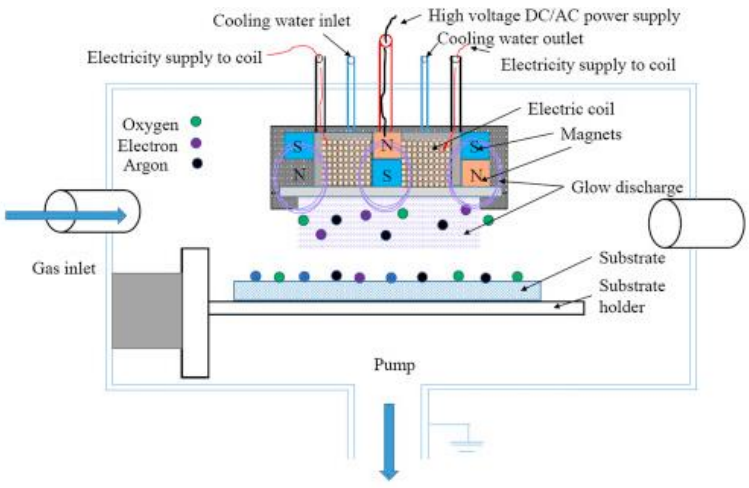

Figure 20 Illustration of Sputtering Chamber [72].

2.2.11 Scanning Electron Microscope

A scanning electron microscope (SEM) utilized accelerated high energy electrons (1-30 kV) to observe and characterize materials in the scale of a nanometer (nm) to micrometer (µm) by using high magnification [73]. The targetted sample area is scanned with a finely focussed electron beam. The beam of electrons collects signals from the sample by interacting with the surface to create an image of surface topography, crystallography, or elemental composition analyses using energy-dispersive spectroscopy (EDS). Various types of signals interact with the sample and give information from different volumes of the specimen. The signals can be secondary/backscattered electrons, and characteristic x-rays [73]. Secondary electron and backscattered electrons are used for surface topography and characteristic x-rays to analyze quantitative and qualitative information [74]. Throughout the project elemental analyses of the thin films were done by Energy-dispersive X-ray spectroscopy (EDS) which allows for quick, quantitative, non-destructive, low-cost examination. Studying the outer layer and acquiring its composition is feasible by altering the beam energy. The lower detection limit is determined by combining the components in the sample's X-ray energy characteristics and the detector's properties. This study is performed with 15 keV accelerating voltage, at a 7 mm distance and at 5kx magnification to resolve profile and deposition heterogeneities. The used SEM-EDX is from Jeol-FE-SEM SUPRA 35 VP.

Figure 21 Jeol-FE-SEM Supra 35 VP.

2.2.12 Profilometer

The profilometer extracts the surface profile by contacting a very fine and sensitive probe onto the material's surface to elicit topographical information. The objective of the device includes measuring surface roughness, morphology, and step height meaning, the thickness. The stylus movements are converted to a graph for the analyses. The profilometer is from KLA-Tencor P-6. It is used to measure thicknesses of the produced thin films during the project.

Figure 22 Profilometer KLA-Tencor P-6.

2.2.13 Variable Angle Spectroscopic Ellipsometer

The instrument of variable angle spectroscopic ellipsometer (VASE) used is the J.A. Woollam Co., Inc., VASE VB-400. Ellipsometer characterizes materials by using polarized light by the phase change of the reflected or transmitted light beam from the surface of samples. Measurements are performed using an incident beam of polarized light in the range of 300nm to 1700nm wavelength. The measurements can be done at various angles, in the experiments 65°, 70°, and 75° are used. Brewster's angle is the incidence angle at which light of a specific polarization penetrates a clear dielectric surface perfectly without reflection. The angles are chosen to be around Brewster angle, which is 69,9° in air for TiN. The ellipsometric parameters psi(ψ) and delta**(**Δ), are measured in ellipsometry and related to the Fresnel coefficients R_s and R_p for s- and p-

polarized light. Since, the equation is the ratio of two values and results in complex number, it gives accurate and sensitive results on phase information.

$$\rho = \frac{R_p}{R_s} = \tan(\psi) e^{i\Delta} \tag{2.1}$$

It is used to determine film thickness, surface roughness, and optical constants (i.e., refractive index (n) and extinction coefficient (k)) for many types of materials, including multilayers, semiconductors, polymers, metals, and dielectrics between 193 to 3200 nm [75]. Optical properties are not measured directly. They are parameters of functions for the interested value. The obtained data is modeled and fitted to find the values of sample with the WVASE32© program.

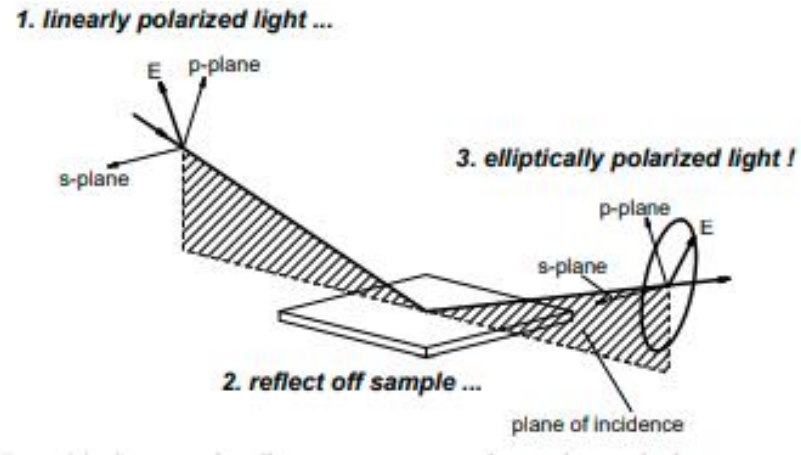

Figure 23 Schematic of VASE showing p- and s- plane directions.

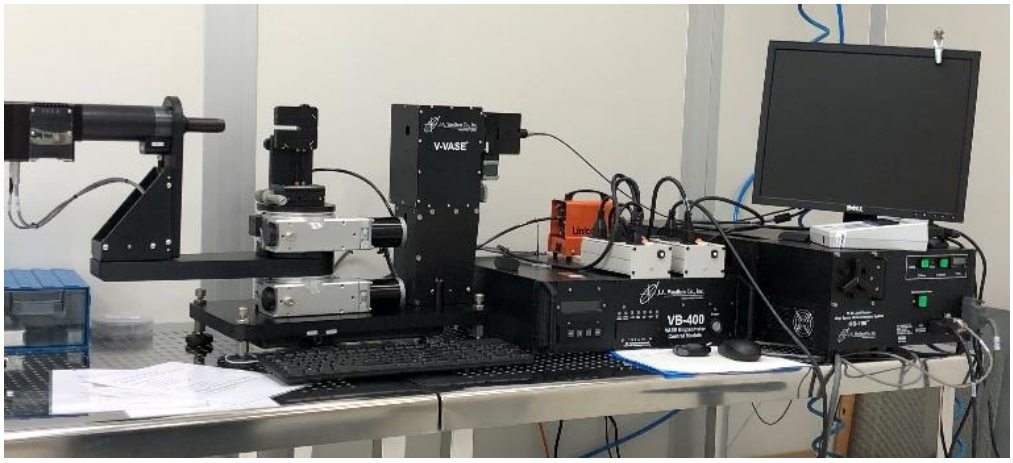

Figure 24 J.A Woollam VASE VB-400 Ellipsometer.

2.2.14 X-Ray Difraction

X-ray diffraction is a non-invasive method that analyzes chemical composition, physical properties, and crystallographic structure. The analyses are performed by an incident x-ray beam focussed in the center of the sample with an angle, and the scattered light with the direction results as intensity. The incoming x-rays irritate crystal atoms and make elastic scattering. This concept is defined by Braggs's law;

$$2dsin\theta = n\lambda \tag{2.2}$$

From the formula, diffracting planes distance is d, the angle of coming light is θ, the wavelength of the beam is λ, and n is an integer [41]. The sample is brought parallel to the stage, and the formed X-ray beam hits onto the sample, and the diffracted light is collected with the detector. The sensed data are fit onto a spectrum analysis, and information is gathered from the sample. In this study, the obtained thin films by reactive sputtering are evaluated with the CuKα1 (1.540 Å) source. The measurements are conducted between angle range of 20<2θ<80, in steps of 0.02^{o} with Bruker D2 Phaser. Consequently, an X-ray diffraction beam can obtain the crystal structure of a material in this study to confirm the crystal structure of TiN.

Figure 25 Bruker D2 Phaser XRD.

2.2.15 Raman Spectroscopy

Raman spectroscopy is a non-invasive chemical analysis method that may provide insides about chemical structure, crystallinity, and molecular interactions. It works on the interaction of light with chemical bonds. A diode-pumped green laser with a 532 nm line at various power levels was applied to characterize thin films. The measurements were in the range of 100-1500 Raman shift (cm^{-1}), 20 seconds, 20 accumulations per area under ambient conditions. For each film, at least 3 regions around the sample were analyzed. All measurements of the samples were conducted under standard conditions using Renishaw InVia Reflex Raman Spectrometer (Renishaw, New Mills, UK).

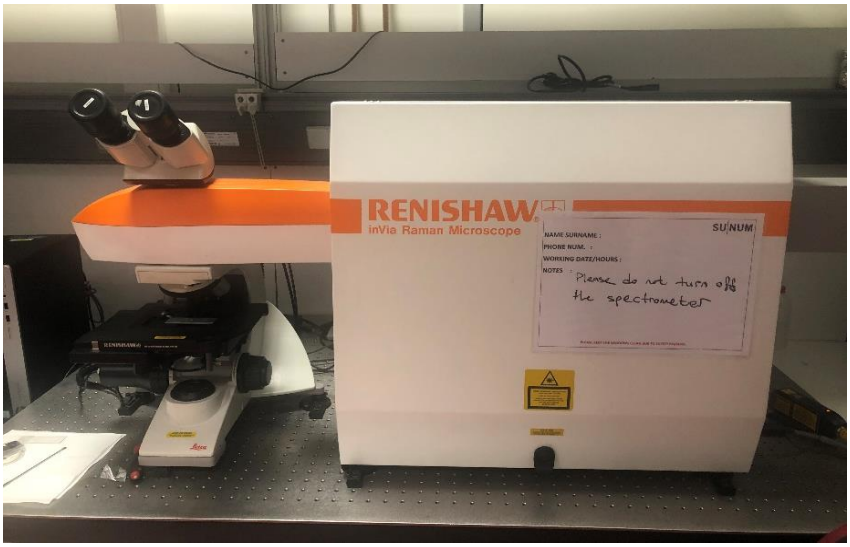

Figure 26 Raman Spectrometer.

2.2.16 Four-Point Probe

The four-point probe method is an impedance recording technique for determining a conductive material's electrical sheet resistance. It is an electrical characteristic used to characterize thin films of conducting and semiconducting materials, indicated by the symbol ohm-per-square (Ω/sq). It is a measurement of the lateral resistance in a thin square of material, between opposing sides of a square. For determining a material's sheet resistance, the four-point probe is the most standard measurement tool to be used. If the thin film has a known thickness, the electrical resistivity [ohm-cm] may be estimated based on the sheet resistance. The functioning concept of a four-point probe is shown in

Figure 28. A DC current is driven via force probes, the two outside probes, force probes. The two inner probes, sensing probes, measure the voltage. With equal spacing between the four probes, this analysis can be performed. To reduce the voltage between two probes, a current is supplied via the outer two probes. The sheet resistance will then be determined by observing the voltage drop [76]. From the formula [77], inner probe voltage is (V), outer probe current is I (A), the sheet resistance is ρ_s (Ω.sq).

$$\rho_s = \frac{V}{I} 4.5324[\Omega/sq] \tag{2.3}$$

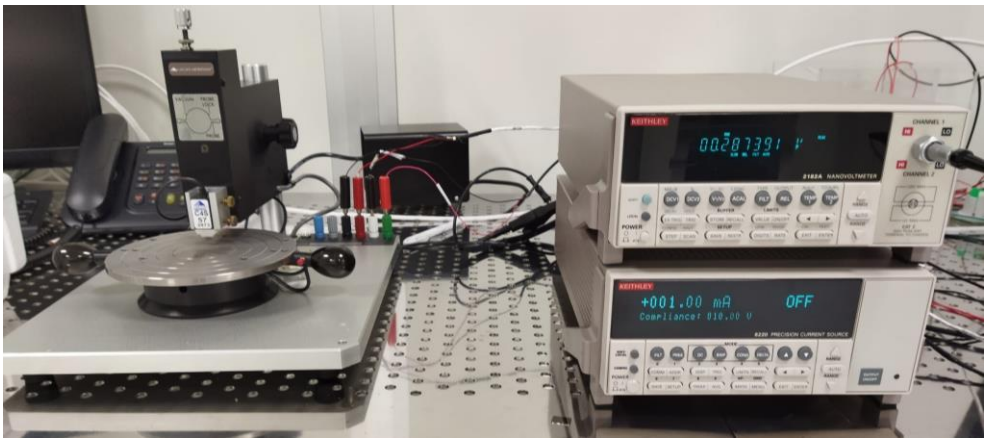

Figure 27 Keithley 2182A nanovoltmeter.

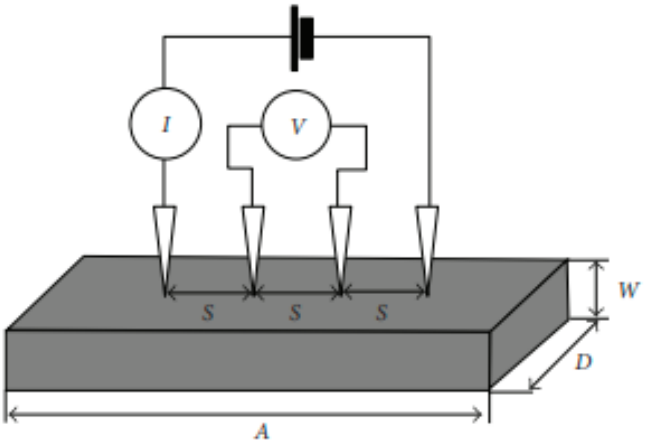

Figure 28 Diagram of four-point probe method [77].

3 RESULTS & DISCUSSION

This section of the thesis will start with the nanosphere lithography studies' etching, and will be discussed with the SEM images of the surfaces, which were coated with aluminium for optimization. Afterwards, the thin film deposition will be given in different approaches to form TiN thin films, done in the cleanroom. These approaches are room-temperature sputtering, purging of argon gas and leaving the system to overnight vacuum, and substrate heated sputtering. Every proposition is changed according to their characterization results and analysis of the deposited samples. Each of them will be discussed under their titles.

3.1.1 Etching Optimization Study for Hexagonal Close-Packed Monolayer

Following the self-assembly technique, the effect of altering the etching duration was investigated using an oxygen plasma asher. Starting with an unetched surface, 60, 90, and 120 seconds were attempted under 40 W plasma power, as shown in Figure 29. All experiments are coated with Aluminium (Al) for the optimization step using the thermal evaporation method. The majority of nanospheres are removed using a tape that is adhered to the substrates, and all substrates are soaked in acetone, methanol, and ethanol for ten minutes each. For Figure 29, plasma power is maintained constant and varied periods were used to determine the best values for nanoarrays. The greater the time during etching, the smaller the nanospheres get. However, after 90 seconds, the form of nanospheres became non-spherical. Since, physical and geometrical characteristics affect hole form, size, depth, film material, substrate refractive index, and array period, may be used to tailor for instance the EOT spectra [78]. Another method is shown in Figure 30. With 90 second duration, different power levels (20, 30, 40, 50, 60 watt) are explored. Nanospheres begin to lose their circular form as power strength increased. The lower the

power, results in better precision of etching. However, below 40 watt, plasma reflection occurred. Since spheres were identical in diameter and decreased linearly, the experiments proceeded with 40 watt and increasing time (120, 150, 180, 210, and 240 seconds), as seen in Figure 31. The hole shape and array order affects optical responses, influences the wavelength and strength of the resonance, so the optimum process was found to be at 40 watt and 210 seconds.

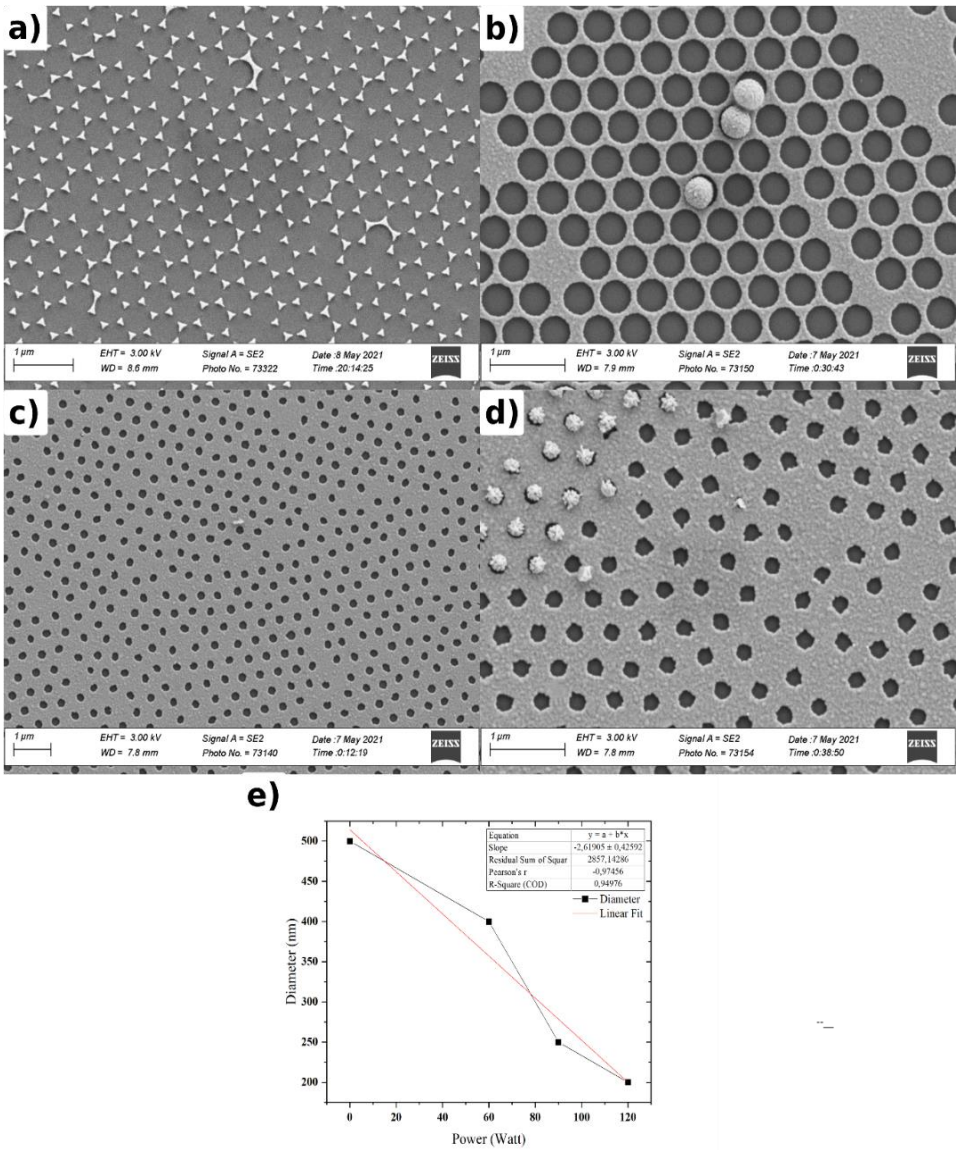

Figure 29. 500 nm PS diameters of nanoarrays. a) unetched, b) 60 s, hole diameter 400 nm. c) 90 s, hole diameter 250 nm. d) 120 s, hole diameter 200 nm.

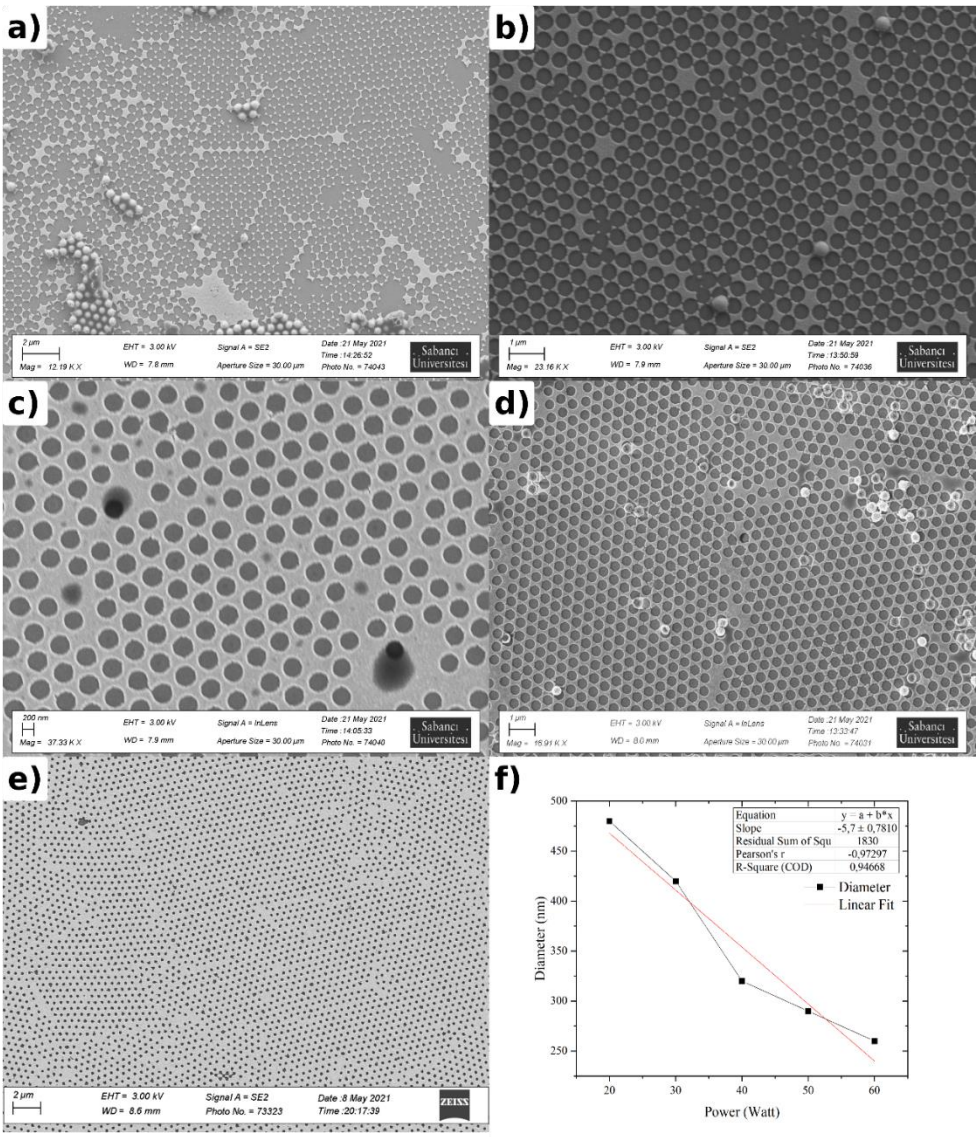

Figure 30 Different power levels a) 20, b) 30, c) 40, d) 50, e) 60 watts at 90 seconds, f) graph for diameter and power relation.

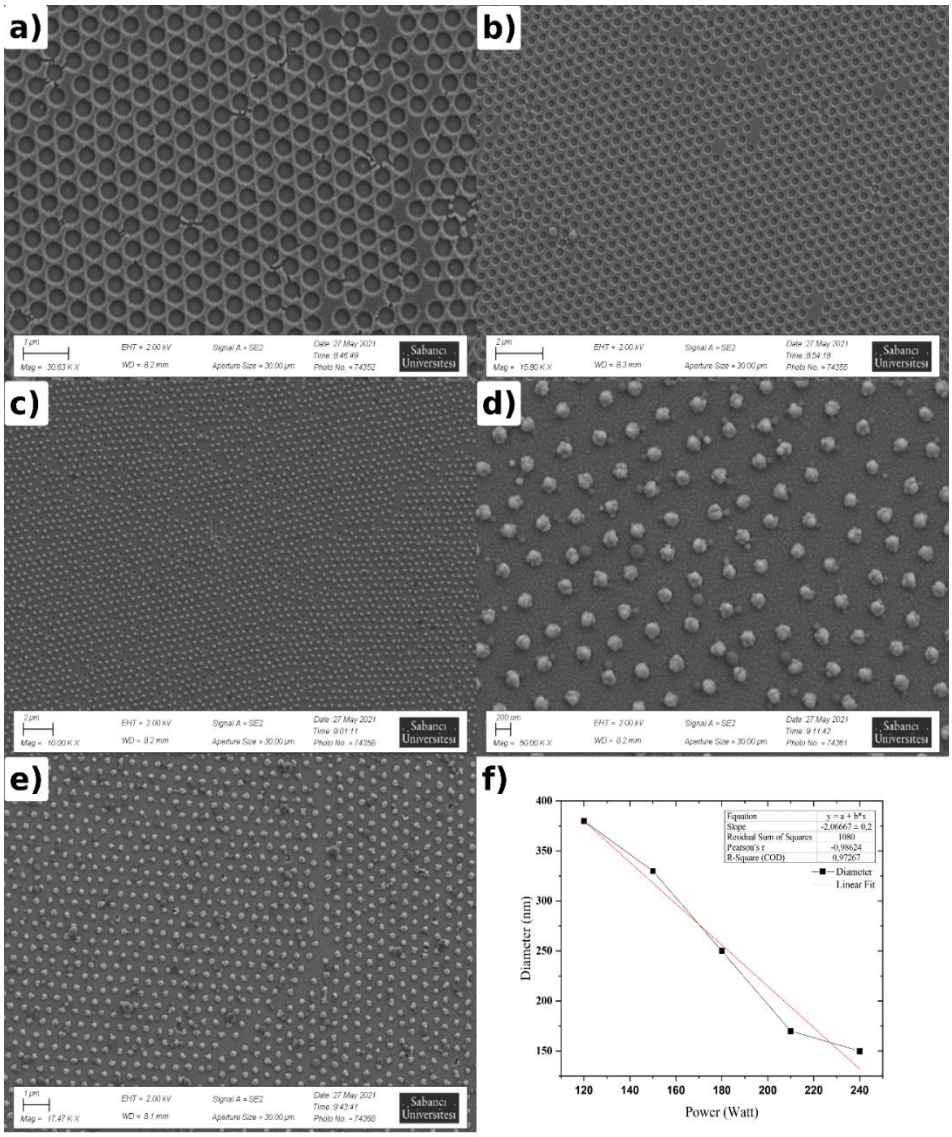

Figure 31 40 watts and increasing durations a) 120, b) 150, c) 180, d) 210, e) 240 seconds, f) graph for diameter and time relation.

3.2 Thin Film Deposition for Titanium Nitride

The deposition factors considerably impact thin films' electrical, mechanical, optical, and morphological characteristics. Important factors include the reactive gas flow and partial pressure, total pressure, deposition temperature, and sputtering power. The chamber pressure influences the kinetic energy of the source atoms impinging on the expanding thin film. By varying gas pressure, the kinetic energy of the atoms may be adjusted [79]. Because energy is lost via greater collisions and interactions of the particles on their way

to the substrate, an increase in pressure lowers the total energy at the substrate. When the system vacuum is reached (system pressure $\approx 5.10^{-6}$ Torr), gases (Ar and N_2) flow into the chamber, achieving greater pressure while coating on the order of 10^{-2} Torr. The target holder, which is the cathode, is subjected to a strong alternating current voltage. In depositions, argon gas forms the plasma for target ignition and system cleaning to remove particles that lead to contamination. Since it is an inert gas that, does not react with either the target or the developing layer, which is ideal for the ignition process, nitrogen is introduced to the chamber after the pressure stabilizes. Due to the strong electric field, the plasma is ignited, ionizing the gas atoms and driving them towards the cathode, where the metallic target (Ti) is located. Along with the electric field, magnetrons located inside the target holder are used to activate a magnetic field in addition to the electric field. A magnetic field raises plasma density and limits it to a zone around the metallic target, enhancing sputtering efficiency. The collision rate of diffusing sputtered atoms depends on the pressure in the chamber, which is determined by the gas flow. Firstly, lower pressures result in a fall of the collision rate since fewer ionized atoms are available to impact the target in the chamber. Secondly, higher pressures increase collision rates the number of particles that reach the substrate, resulting in a lower deposition rate due to reduced mean free path of the particles. In the deposition step, the employed sputtering system has three sources; two DC and one RF, and each can sputter one element. All processes are done under reactive RF magnetron sputtering. Zirconium (ZR) target is used on DC magnetron for system cleaning purposes. An electronic-controlled rotating plate in the sputtering chamber, the sample holder, is fixed and rotated for the substrate to be equally coated. This allowed to put the sample holder on top of the system and then deposit each source one at a time, maintaining the vacuum in the chamber. Once the deposition step starts, the sources are ignited, and a monitor controls the system.

3.2.1 Results for Samples Sputtered at Room Temperature

The first optimization studies for titanium nitride (TiN) films were deposited on cleaned (100) silicon wafer and soda-lime glass substrates, as described in 2.2.1 Substrate Preparation, using room temperature reactive RF magnetron sputtering. The deposition was carried out using a titanium metal target with a purity of 99.99%. Nitrogen gas is pumped into the system. Before deposition, the pressure within the chamber was adjusted

to 25 mTorr for ignition and then decreased to 20 mTorr. The deposition rates, thicknesses, and parameters of the films are shown in Table 1 and Table 2. Plasma power, deposition time, system pressure, and other details of the deposition process, except gas flows were kept constant for all the samples in a set.

Table 1 Deposition rates and thicknesses for samples sputtered at room temperature.

N_2(%)	Ar (sccm)	N_2 (sccm)	Deposition Rate (Å/s)	Thickness (nm)
5	7.3	0.4	0.2	200
7	7.2	0.5	0.1	80
10	7.2	0.8	0.1	72
20	6.2	1.5	0.09	65
30	5.7	2.4	0.06	53
40	4.8	2.2	0.02	20

Table 2 Experimental values for samples sputtered at room temperature.

Parameters	**Values**
Sputtering temperature	Room temperature
Deposition time	20 minutes
Base pressure	$5x10^{-3}$ Torr
Power-pressure	200 W@ 20 mTorr
N_2 concentration	40, 30, 20, 10, 7, 5%
Target	Titanium

The color of the coatings, shown in Figure 32, can be related to the thin-film interference as well as its XRD results in 3.2.3. Incident light strikes onto the deposited thin film partly reflected and refracted from the surface. Refraction occurs by the reflection from the bottom part. Both radiations interfere depending on the thicknesses and refraction indices of the medium. When light enters the film, it travels a distance and can be in or out of the phase with the light reflected from the surface. The thinnest the film, the darker it will be. The color is indirectly related to the wavelength (λ) of light and thickness (t). At different thicknesses, colors change. If medium's refraction index is higher than the medium, phase change will occur, shifting by $\lambda/2$. When the film is thin, the difference in the length of a distance of the two rays traveled will be negligible. They will be out of phase leading to destructive interference, being darker. The constructive interference will be in-phase and

will show brighter colors. The thicknesses of films are measured with a profilometer and are given in Table 1.

Figure 32 The colors of silicon wafer substrates deposited with various N_2 partial presssures: 40%, 30%, 20%, 10%, 7%, 5% from left to right respectively.

3.2.2 SEM-EDS Analysis for Samples Sputtered at Room Temperature

Energy dispersive X-ray spectroscopy (EDS) was used to characterize the composition of the deposited thin films. EDS is highly sensitive to characteristic X-rays which shows the present elements in the specimens. As shown in Figure 33 three elements were mapped along the surfaces: titanium, nitrogen, and oxygen. With the increasing nitrogen pressures, oxygen shows an increasing trend while titanium and nitrogen show a decrease in their atomic percentages. EDS scan shows that oxygen is present throughout the set and has the highest atomic percentage, this states the chamber of sputter was contaminated. The observation is that produced films under room temperature condition resulted with high content of oxygen (O_2) gas due to the leakage to the system and the usage of many different materials by other users of the sputter. Further, the colors of silicon substrates proved that the films are not TiN but rather oxygenated samples. The colors differ according to their thicknesses. Although EDS method is not enough to confirm definite proportions of elements, from the darker color (60/40) which has the highest oxygen amount as shown in Figure 32, the samples can be concluded as titanium monoxide, TiO_y [80].

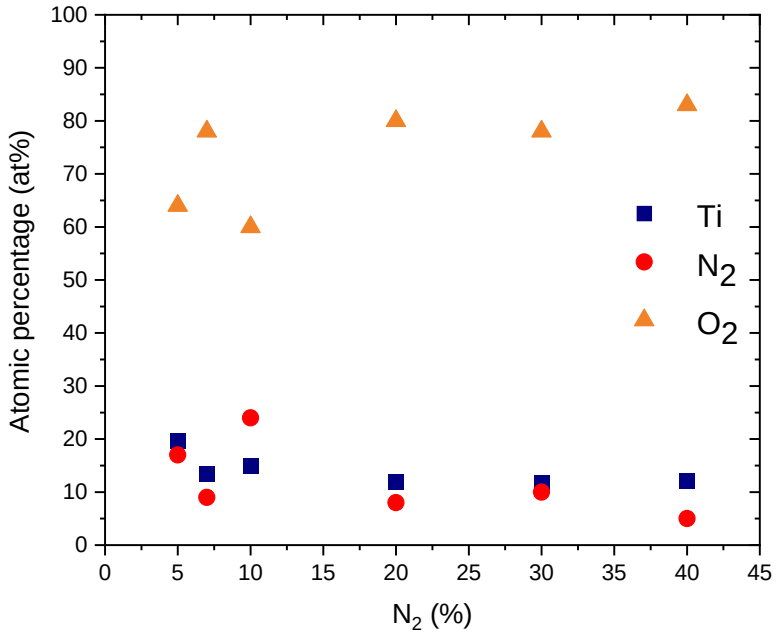

Figure 33 Atomic percentage graph for each element compared with th increase in N_2.

Table 3 Elemental analysis of room temperature depositions with different N_2 partial pressures given in weight percentage.

Elements (wt %)	**60/40**	**70/30**	**80/20**	**90/10**	**93/7**	**95/5**
Ti	30.35	28.35	29.78	36	32	43.02
N	4.03	7.68	5.48	16.6	6.38	10.86
O	65.62	63.96	64.74	48.8	61.92	46.12

3.2.3 XRD Analysis for Samples Sputtered at Room Temperature

During the XRD experiments, the incidence and refracted angles are determined. A distinctive x-ray diffraction pattern is formed by graphing the recorded x-ray intensity as a function of angle [81]. The XRD pattern for the samples generated by reactive sputtering at the various composition of Ar/N_2. Peak intensities at different diffracted angles are utilized to determine the crystallographic orientations of the material under examination. The intensity is defined as the entire area enclosed by a peak. XRD analyzes of the produced films are given to understand crystal structure. The x-ray diffraction (XRD) spectra of TiN films sputtered on different substrate surfaces, silicon wafer and soda-lime glass (SLG). It was observed on glass substrate produced films resulted in amorphous

structure. Due to titanium and nitrogen atoms, which react during the formation of thin films, did not form TiN, instead, the XRD spectra showed oxidized samples which are formed while sputtering [82]. There are four distinct phases of titanium monoxide (TiO) as found from the literature: cubic TiO with a rock-salt structure (a = 4.174), ß-TiO with a superstructure of rock-salt TiO (a = 12.54), monoclinic α-TiO (a = 5.860, b = 9.340, c = 4.141, =107.553°), and hexagonal ε-TiO (a=4.9936, c=2.8773°). The nonstoichiometric compound that makes up the rock-salt TiO phase has a composition range of $TiO_{0.7}$ to $TiO_{1.25}$. Even in crystal lattices, there are a lot of vacancies. As a result, synthesizing substantially pure rock-salt TiO and TiN samples is challenging under these circumstances [83]. In Figure 35 and Figure 36 the major peaks are given according to their substrate. The black bars depict Bragg sites for rock-salt TiO with a structure similar to sodium chloride (NaCl) (PDF-01-0993-halite). The cubic TiO crystal structure, in which the red dots represent oxygen and the pink dots symbolize titanium atoms, is of the NaCl type in Figure 34. The increase or decrease of nitrogen in the plasma composition did not show any enhancement in the formation in the TiN phases for room temperature sputtering in the system used. The reason of NaCl peaks is because low quality grade silicon was used and it was used as it arrived. However, glass substrates were washed with alcohol beforehand, so sharp peaks of NaCl cannot be seen.

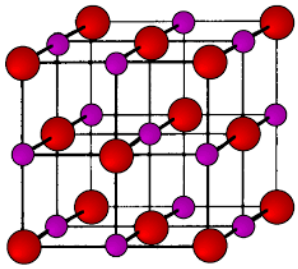

Figure 34 The cubic crystal structure of both TiN and NaCl.

Table 4 XRD angles and phases for TiO_x.

Angle (2θ)	**Phase**
36°	(111)
43°	(002)
62°	(022)

Table 5 XRD angles and phases for NaCl (halite).

Angle (2θ)	Phase
28°	(111)
32°	(200)
45°	(220)
53°	(311)
56°	(222)
65°	(400)

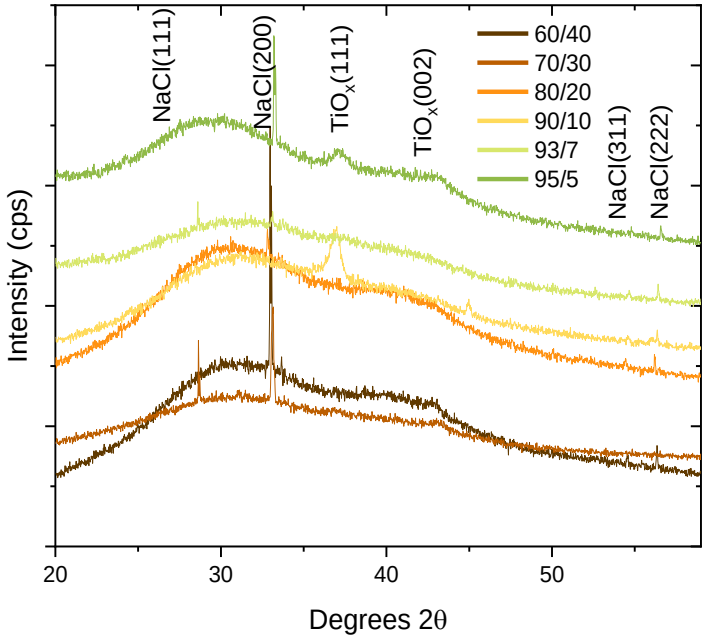

Figure 35 XRD pattern of TiO (NaCl-type) deposited on silicon substrates with varying compositions at room temperature.

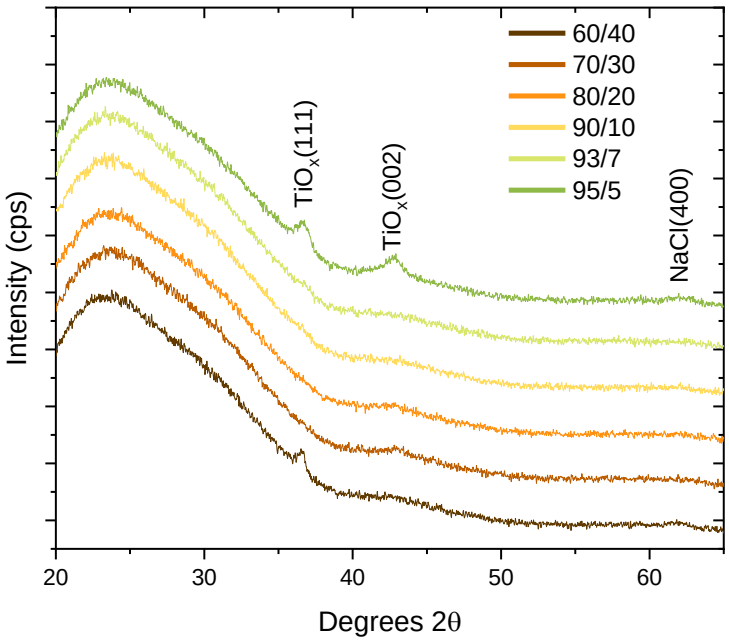

Figure 36 XRD pattern of TiO (NaCl-type) deposited on glass substrates with varying compositions at room temperature.

3.2.4 Raman Analysis for Samples Sputtered at Room Temperature

In most circumstances, the degree of crystallinity in a material is sensitive to Raman scattering. A crystalline material's spectra will typically have highly sharp, strong peaks, while an amorphous material's spectrum would have wider, less intense peaks. These two states might be regarded spectral extremes, and a Raman spectrum from an intermediate state, semi-crystalline, will have intermediate peak strength and width. It has been reported that even in stoichiometric TiN, both Ti and N vacancies exist. The existence of point defects eliminate the inversion symmetry, permitting first-order Raman scattering. Therefore, the first-order Raman spectra is related to the point defects. The form of first-order Raman spectra will be approximately proportional to the phonon density of states [84]. Raman spectra of both substrates silicon and glass are examined. The vibrations of Ti ions are determined by the scattering in the acoustical range, whereas optical range is within the vibrations of the N ions. The intensity ratio of acoustical to optical scattering is a measure for Ti:N stoichiometry. Two broad peaks are observed one between 250 and 400 cm^{-1} and second between 650 and 850 cm^{-1} for silicon substrates. The first-order

longitudinal acoustic peak LA(285 cm^{-1}) occur due to the nitrogen vacancies, leading titanium atoms to large intensity peaks. Since these samples are not stoichometric, multiphonon peaks 2TA(400 cm^{-1}), LA+TA(500 cm^{-1}), 2LA(600cm^{-1}) are not present. The intensity of LA peak decreases with increasing nitrogen percentage. Also, this could be due to the oxygen presence in the samples. Other two multiphonon peaks LA+TO(800 cm^{-1}) and second-order 2TO(1100 cm^{-1}) are also shown. There is a broad peak around 800 cm^{-1}, but since the other phonon peaks are not present, it cannot be concluded as stiochiometric. For SLG substrates, there are again two distinct broad peaks one between 570-680 cm^{-1} and other in between 1000-1200 cm^{-1}. First-order vibrations at 280 $cm^{-1}$and 562 cm^{-1} peaks are present related to LA and TO modes respectively. The peak at 1090 cm^{-1} is 2TO [84]. The reason why on glass, amorph material, the peak intensity of transverse phonons is much higher than in silicon is the sensitivity to disorder. This property is lower in longitudinal phonons [85]. Since, Raman measures samples from their surfaces (applied power 5%), these samples showed TiN structure, because this could be due to the formation of nitrogen close to the upper part of surfaces. When compared to XRD results, which shows higher penetration depth than in Raman, nitrogen related peaks are not found. It could also show results related to SiO_2, which can form on the surface of silicon substrates, depending on the thickness of the films.

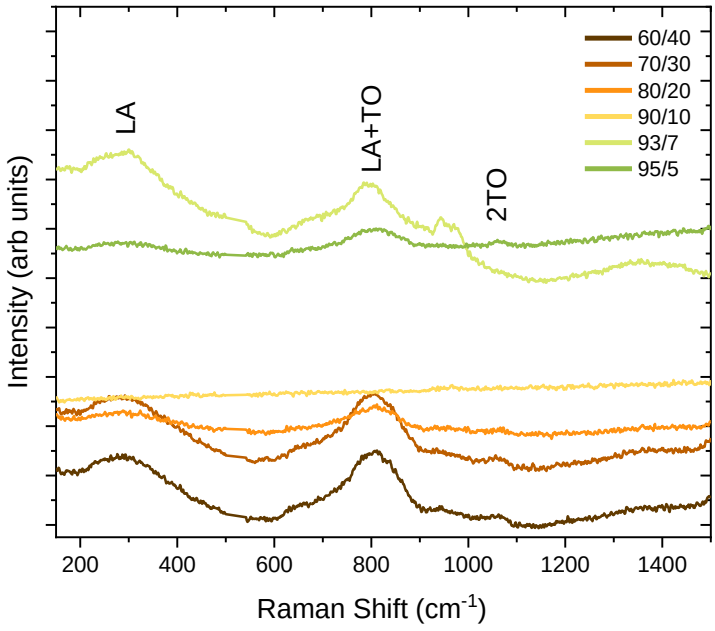

Figure 37 Raman spectra for samples deposited on silicon substrates at room temperature for various compositions of Ar/N_2.

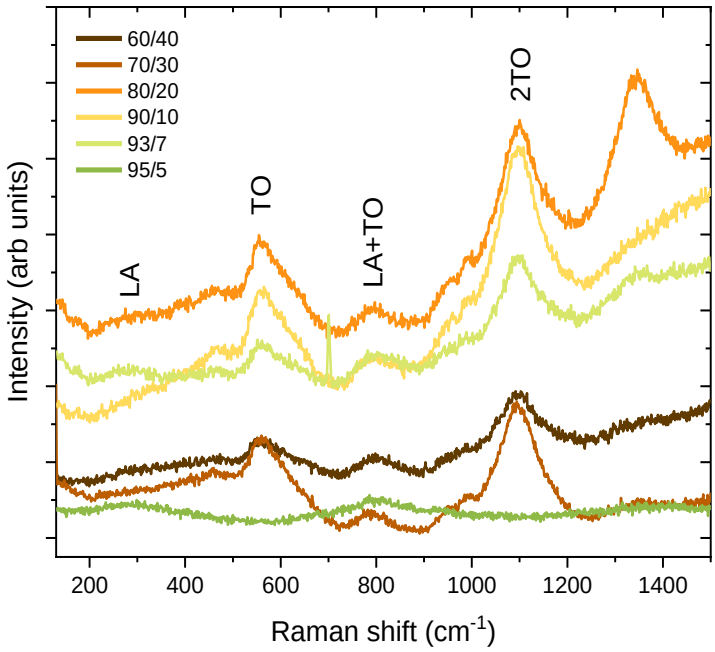

Figure 38 Raman spectra for samples deposited on glass substrates at room temperature for various compositions of Ar/N_2.

3.2.5 Four Point Probe Measurements for Samples Sputtered at Room Temperature

One of the crucial electrical characteristic is defined by sheet resistance (Rs) which is utilized to characterize films of semiconducting and conducting materials. It assesses the capacity of electrical charge that move in the plane of the film and is a measure of lateral resistance per square area of a film with uniform thickness. The four-point probe is the industry standard for testing sheet resistance. All of the samples are measured under 100 mA and in the range of 1V with Keithley™ 2182A nanovoltmeter for the consistency between experiments. However, when 1 mA applied to the samples, these room temperature samples are all exhibited dielectric. When the power of the current is increased, they showed values. With the formula (2.2), the graph below represents the most resistive thin films.

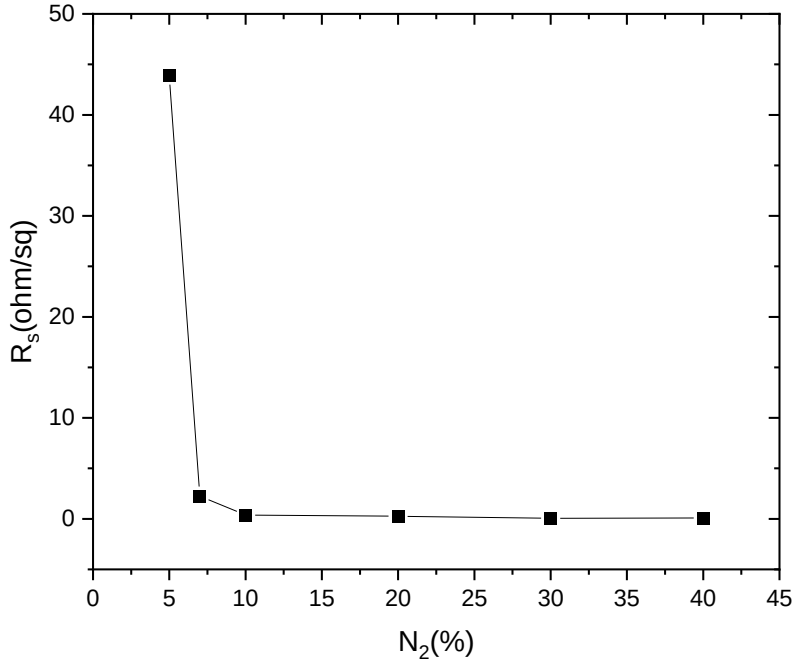

Figure 39 The measured sheet resistances of samples deposited on silicon at room temperature for different nitrogen partial pressures.

3.2.6 Optical Measurements for Samples Sputtered at Room Temperature

Variable angle spectroscopic ellipsometry measurement was presented to reveal optical constants of room temperature sputtered samples. To understand plasmonic characteristics, obtained measurements were fitted to a model to find real and imaginary part of dielectric function. The deposited films were aimed to be TiN. However, applied characterization methods demonstrated different material properties, so knowledge on these films were very limited. B-Spline dispersion model is used in this set with three angles of incidence at 65°, 70°, and 75°. B-spline is a polynomial and uses various nodes to match function and fits $\psi(\lambda)$ and $\Delta(\lambda)$. This model can be fitted to absorbing films. The thickness and refractive index for each sample helps to develop optical model. The model quantitatively indicated the fit quality of the measured spectrum observations. The model's fit is defined by mean squared error (MSE), closer to 1 means it fits perfectly. The values were changing between 1.6 to 6.7. The films were dielectric and transparent on glass substrate. These properties mean they have negligible loss in imaginary part,

varying from 0.8 to 8. Sample 95/5 was colored in metallic and thickness is high than others. Its imaginary part is $\varepsilon'' \approx 8$, the maximum in all six samples, and real part is the highest $\varepsilon' \approx 6$. None of these samples showed plasmonic behavior since real parts are positive.

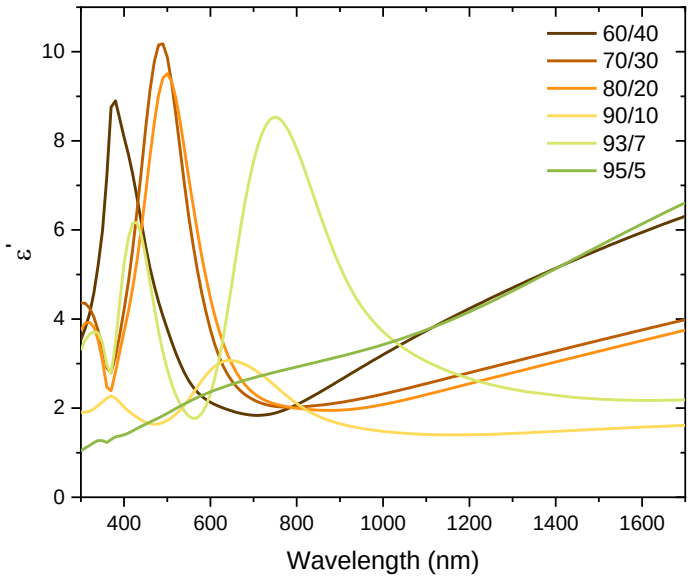

Figure 40 The real part of dielectic function of silicon substrates deposited at room temperature.

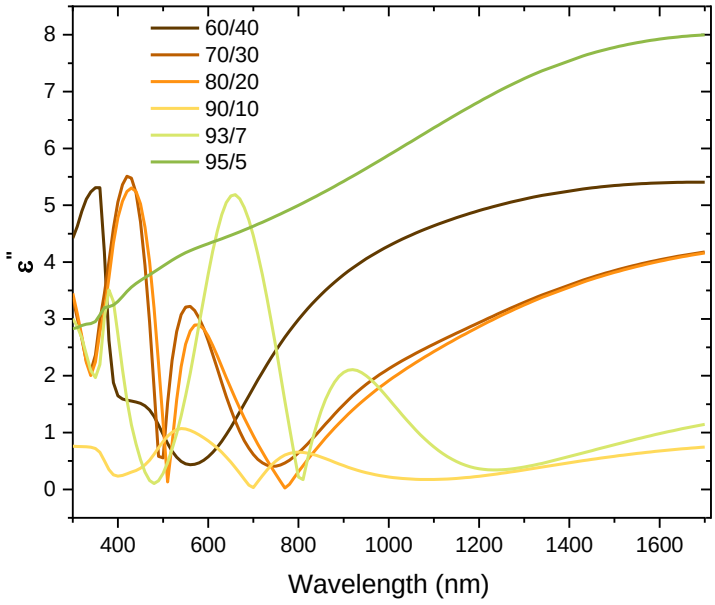

Figure 41 The imaginary part of dielectic function of silicon substrates deposited at room temperature.

3.3 Results for Samples Sputtered After Purging and Overnight Vacuum

3.3.1 Thin Film Deposition for Samples After Purging and Overnight Vacuum

Table 6 Deposition parameters for samples of purged and overnight vacuum.

N_2 (%)	Ar (sccm)	N_2 (sccm)	Deposition Rate (Å/s)	Thickness (nm)	Vacuum Conditions (hr)
10	4.5	0.5	0.7	195	1 hr Ar purge
10	4.5	0.5	0.8	200	1 hr Ar purge+12hr vacuum
20	4	1	0.3	90	12 hr vacuum
20	4	1	0.2	105	1 hr Ar purge+12 hr vacuum
10	4.5	0.5	0.8	150	12 hr vacuum
20	3.1	2	0.5	167	12 hr vacuum
30	3.7	1.6	0.3	200	12 hr vacuum

Table 7 Experimental values for samples sputtered after purging and overnight vacuum.

Parameters	Values
Sputtering temperature	Room temperature
Deposition time	20 minutes
Base pressure	$5x10^{-3}$ Torr – $6x10^{-7}$Torr(overnight)
Power-pressure	200 W @ 15 mTorr
N_2 concentration	30, 20, 10%
Target	Titanium

To achieve lower content of oxygen, purging the system with Argon before deposition for an hour and leaving it to overnight vacuum were the next treatment approaches to increase efficiency as much as possible. This thought to be the solution for the removal of other contaminants from the system. After the overnight vacuum, the system started at around ~$6x10^{-7}$ Torr and when the sputtering started pressure of the system raised to $5x10^{-3}$ Torr. Compared to the first set of experiment, pressure decreased from 20 to 15 to increase deposition rates and thicknesses. SEM-EDS method used to monitor the element contents (Ti, N_2, O_2). After the results of XRD and EDS analysis from the first set, other approaches had been tried to avoid and minimize oxygen content from the chamber. All parameters for these two propositions are given in the Table 7.

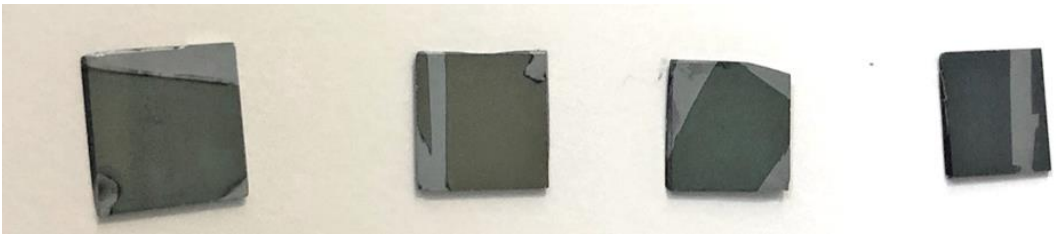

Figure 42 The colors of silicon wafer substrates deposited with various N_2 partial presssures: 90/10 purge, 90/10 purge+overnight, 80/20 overnight, 80/20 purge+ overnight from left to right respectively.

3.3.2 SEM/EDS Analysis for Samples Sputtered After Purging and Overnight Vacuum

For these sets of experiments, EDS analysis showed better results than the first set of experiments. Comparing purging and purge plus overnight vacuum samples with the enhanced vacuum condition was expected to have lower atomic oxygen percentage in 90/10. However, it did not show any improvements. For the 80/20 samples, it was first left to overnight vacuum and then tried under purging and overnight vacuum. In these sets, the results are slightly better than 90/10 but both of the conditions are not much different than each other in terms of oxygen issue. From Figure 42, darker colors shows the oxygenated films. To evaluate the effect of 12 hr vacuum, 10%, 20%, 30% N_2 partial pressures are assessed. The outcomes of this study guided us to try another method, which will be explained in 3.4.

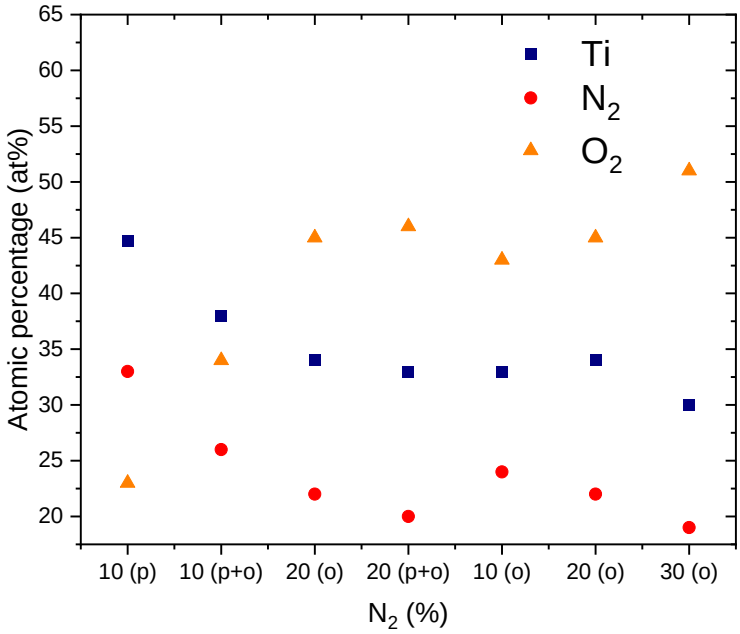

Figure 43 Atomic percentage for each element depending on the vacuum condition.

Table 8 Elemental analysis of purging and overnight vacuum in weight percentage

Elements (wt %)	90/10 (p)	90/10 (p+o)	80/20 (o)	80/20 (p+o)
Ti	72.2	67.05	61.5	61.48
N	15.8	13.12	11	10.56
O	12	19.38	27.4	27.96

3.3.3 XRD Analysis for Samples Sputtered After Purging and Overnight Vacuum

The aim is to purge the system with argon so minimize the oxygen contamination to observe crystalline peaks. However, the contamination did not decreased much to improve crystallinity. The peaks' profile show broad spectrum and sodium chloride peaks were observed again. Overnight vacuum did not show enhanced crystallinity when compared with purging. The deposited samples showed amourphous characteristic again.

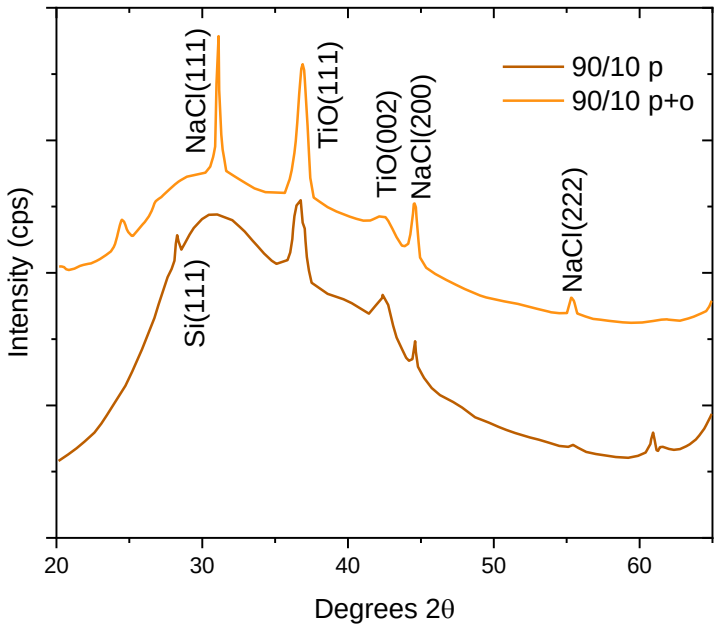

Figure 44 XRD pattern for 90/10 composition samples deposited on silicon with different oxygen elimination methods; p (purging), p+o (purging+overnight vacuum).

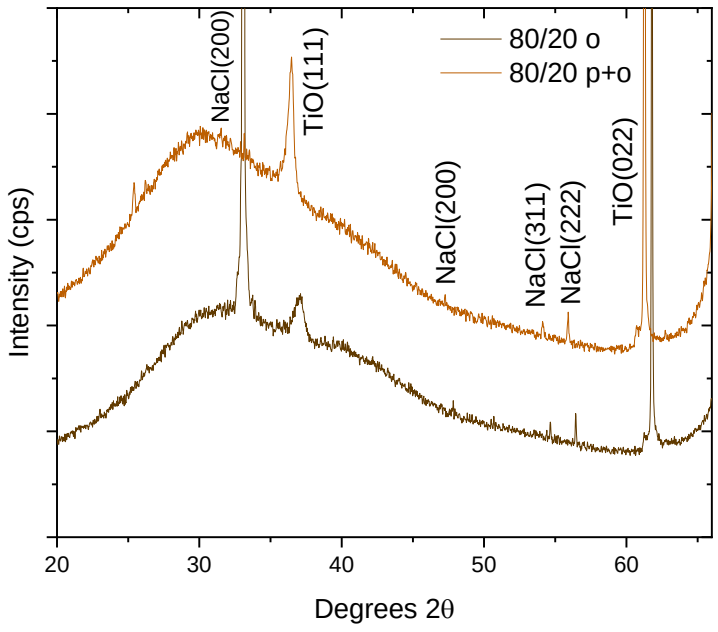

Figure 45 XRD pattern for 80/20 composition samples deposited on silicon with different oxygen elimination methods; o (overnight vacuum), p+o (purging+overnight vacuum).

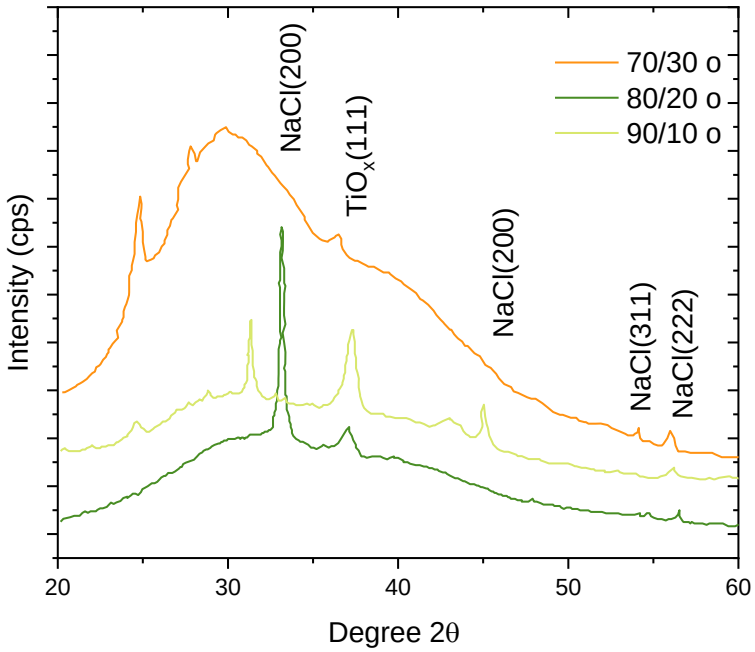

Figure 46 XRD pattern for three different composition samples deposited on silicon after overnight (12h) vacuum.

3.3.4 Raman Analysis for Samples Sputtered After Purging and Overnight Vacuum

Raman spectrsocopy with its sensitivity shows the points defects in transition metal nitrides. The spectra for both substartes includes doublet at low frequencies (below 350 cm-1), which are transverse (TA) and longitudinal acoustic (LA) modes respectively. The peaks are broad in the graph which is the profile of amorphous materials. A peak is observed at 520 cm^{-1} belonging to silicon, because of the thickness. There is a peak around 520-580 cm^{-1} of transverse optical (TO), which shows the titanium vacancies.

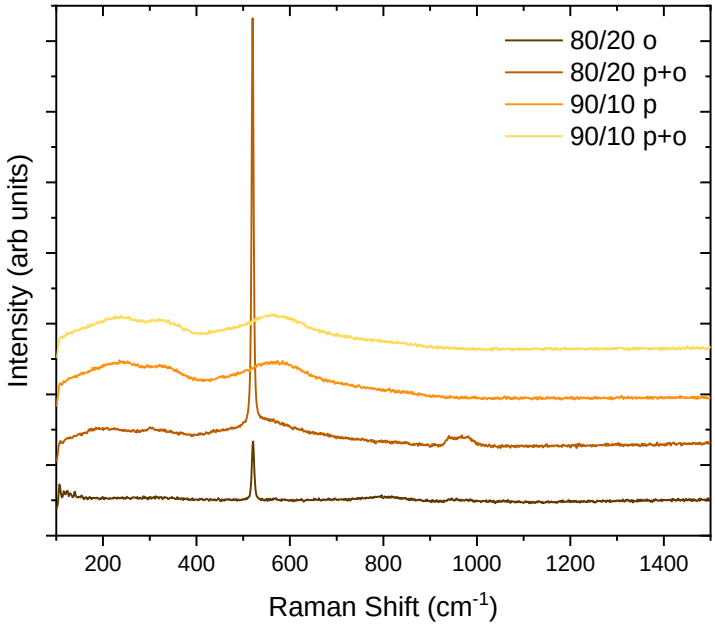

Figure 47 Raman spectra for samples deposited on silicon substrates after purging and overnight vacuum.

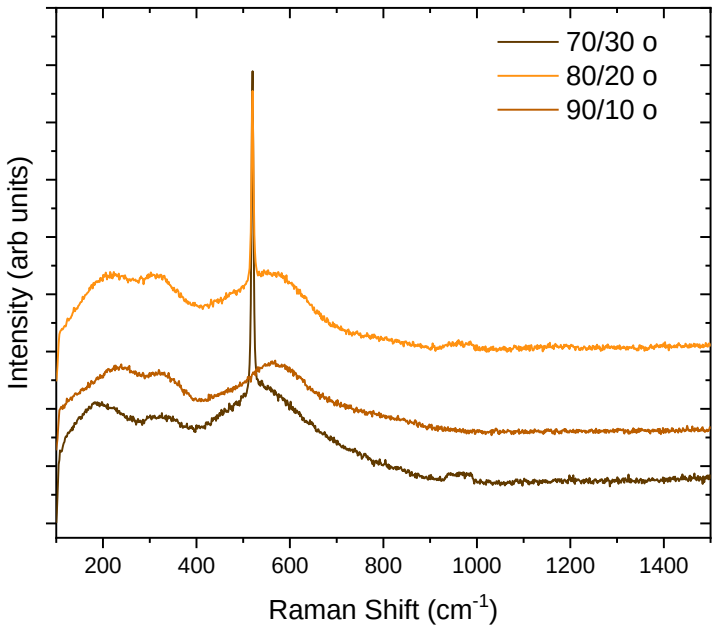

Figure 48 Raman spectra for samples deposited on silicon substrates after overnight vacuum.

3.3.5 Four Point Probe for Purged and Overnight Vacuum Sputtered Samples

From Figure 49, the conductivity increases with increasing nitrogen partial pressure. The samples still show high resistances. Longer time in the system for higher vacuum did not show better results in terms of lowering oxygen and thus increasing conductivity. The sample 80-20 (Ar/N_2) shows higher conductivity, which is related with the thickness of the film.

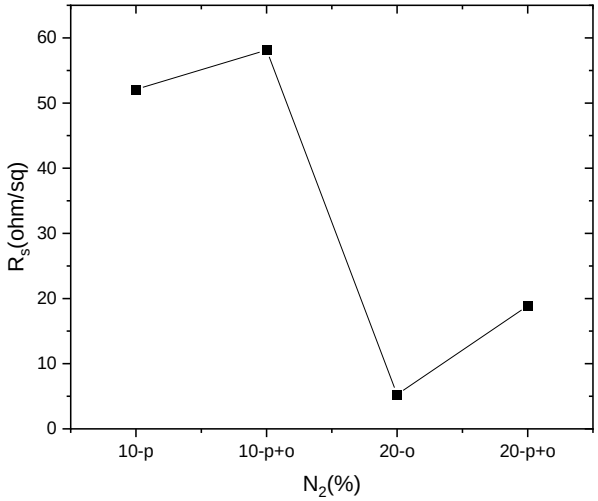

Figure 49 Sheet resistance graph for samples sputtered after purged and overnight vacuum.

3.4 Results for Samples Deposited Under Substrate Heating

3.4.1 Thin Film Deposition for Samples Under Substrate Heating

Table 9 Deposition Parameters Sputtering under 200°C.

N_2	Ar (sccm)	N_2 (sccm)	Deposition Rate (Å/s)	Thickness (nm)
10	2.4	0.3	0.28	312
20	5.8	1.5	0.11	127
25	1.4	0.4	0.86	930
30	1.2	0.5	0.52	570
35	1.1	0.5	0.36	396
40	0.9	0.6	0.28	313
45	1.6	1.3	0.14	160
50	1.1	1.1	0.04	45
55	0.8	1	0.17	194
60	0.8	1.1	0.27	298
65	0.7	1.3	0.12	140
70	0.1	1.6	0.20	221

*All of the coatings are done under substrate heating at 200 ºC.

*All of the experiments above are cleaned prior to deposition with Zirconium for 30 minutes.

Table 10 Deposition Parameters for Sputtering Under Substrate Heating.

Parameters	**Values**
Sputtering temperature	200^{o}C
Deposition time	180 min
Base pressure	$5x10^{-2}$ Torr
Power -pressure	200 W @ 10 mTorr
N_2 concentration	70,65,60,55,50,45,40,35,30,25,20,10%
Target	Zr, Ti

In this sputtering method, different than other sets lower pressure and substrate heating were tried to increase deposition rates and minimize oxygen content in the chamber. The zirconium plasma cleaning is done with DC magnetron. Zirconium is used because it is highly tendent to form bond with oxygen. All of the depositions were coated for 3 hours but since the gas flows were not controlled thicknesses vary form from 40 to around 900 nm.

3.4.2 SEM/EDS Analysis for Samples Deposited Under Heating

The prior cleanning with zirconium and heating of the substrates proved that contaminations could be lowered. Below graph Figure 51 shows the lowest content when compared to other sets discussed earlier. Under heating molecules in the chamber got mobile and with the high vacuum, they are pumped out of the system. Another proof is TiN normally shows gold-like yellow color. However, we did not observe in the sets before, until this one. The colors of the surfaces become rose-gold which proves the decreased oxygen content.

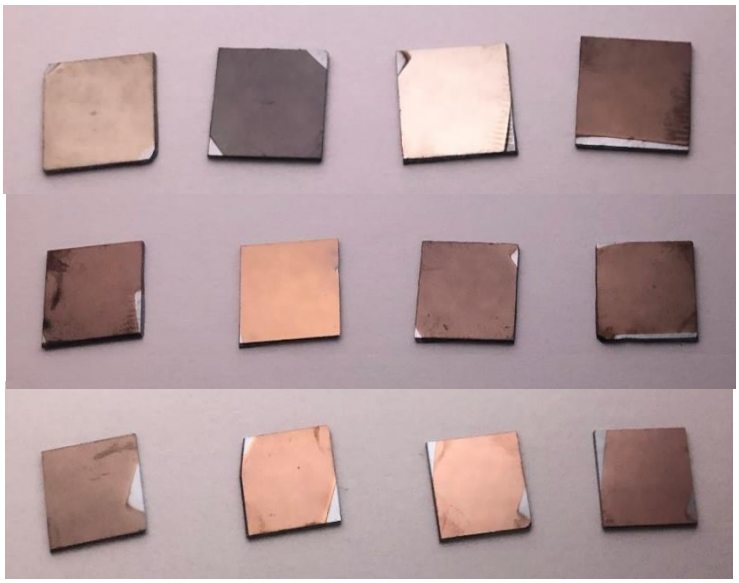

Figure 50 The colors of silicon wafer substrates deposited with various N_2 partial presssures: starting from upper left 10% to 70% in order.

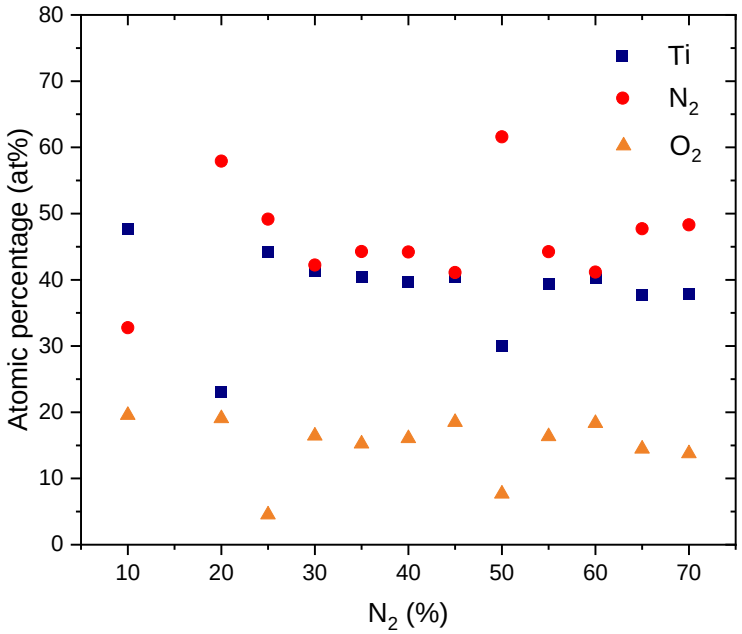

Figure 51 Atomic percentage of samples sputtered under heating.

Table 11 EDS analysis for substrate heated samples.

Elements (wt %)	90/10	80/20	75/25
Ti	74.38	49.92	73.17
N	14.96	36.85	23.82
O	10.21	13.83	2.51
	70/30	65/35	60/40
Ti	69.84	69.7	68.44
N	20.87	22.29	22.29
O	9.29	8.77	9.27
	55/45	50/50	45/55
Ti	68.92	59.8	68.18
N	20.52	35.2	22.37
O	10.56	5.02	9.45
	40/60	35/65	30/70
Ti	68.64	66.63	67
N	23.47	24.84	24.94
O	7.89	8.53	8.15

3.4.3 XRD Analysis for Samples Sputtered Under Substrate Heating

The crystallinity of the thin film is affected by the substrate temperature and sputtering power. The grain sizes become bigger as the temperature rises [79]. The thin film's stoichiometry is influenced by the reactive gas flow and pressure. Argon ions may potentially strike onto the surface expanding film during sputtering. The ratio of ionized atoms to source atoms that strike the expanding thin film has a significant impact on the thin film's shape and crystallites [86]. In general, the greater the deposition temperature, the better the film characteristics, which also leads in a reduced resistance for conducting materials [71]. Since these samples are deposited under 200^{o}C, they exhibited more crystalline compared to other sets of experiments and sharp peaks are observed. As the argon ratio increases (111) peak gets distinct. This shows that there is a correlation between a strong (111) cubic-TiN texture and the stability of the thin film. Unstability can be related to the highly intense (111) texture. From graphs below, it can be seen there is a shift from (111) to (200) texture with nitrogen increase. Unfortunately, NaCl peaks were observed again. From the beginning of this study, low quality silicon wafers were used as they were received.

Table 12 XRD angles and phases for TiN.

Angle (2θ)	Phase
36.5°	(111)
42.5°	(200)
61.6°	(220)
73.8°	(311)
77.7°	(222)

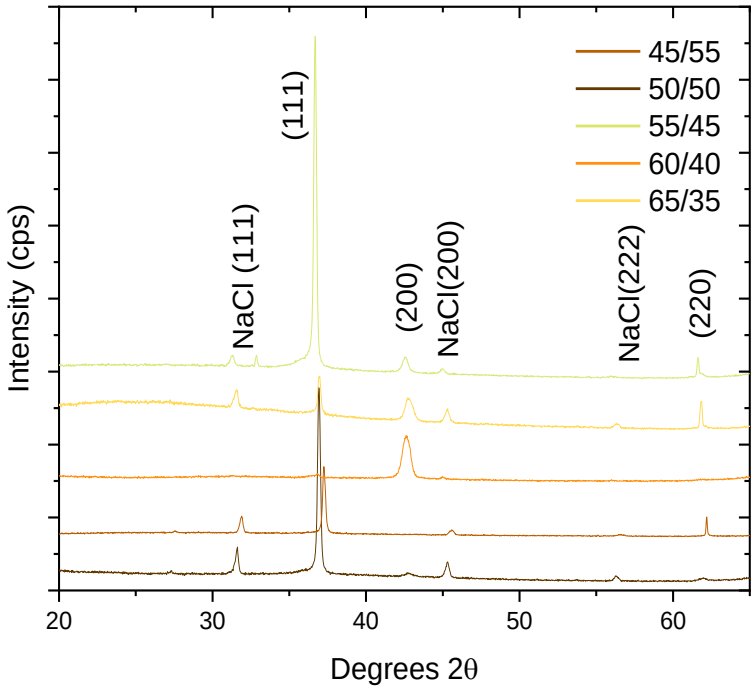

Figure 52 XRD peaks of TiN deposited on silicon substrates under heating for different nitrogen compositions from 35% to 55%.

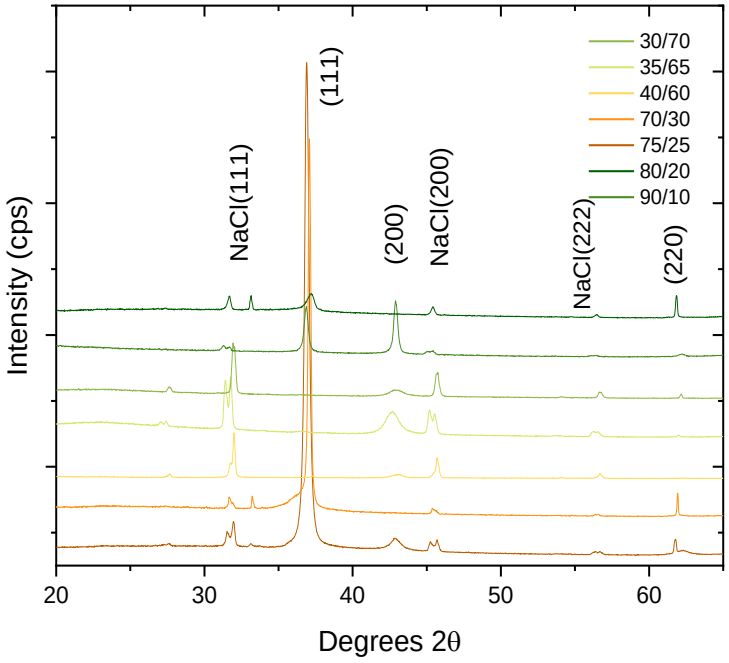

Figure 53 XRD peaks of TiN deposited on silicon substrates under heating for different nitrogen compositions from 10% to 70%.

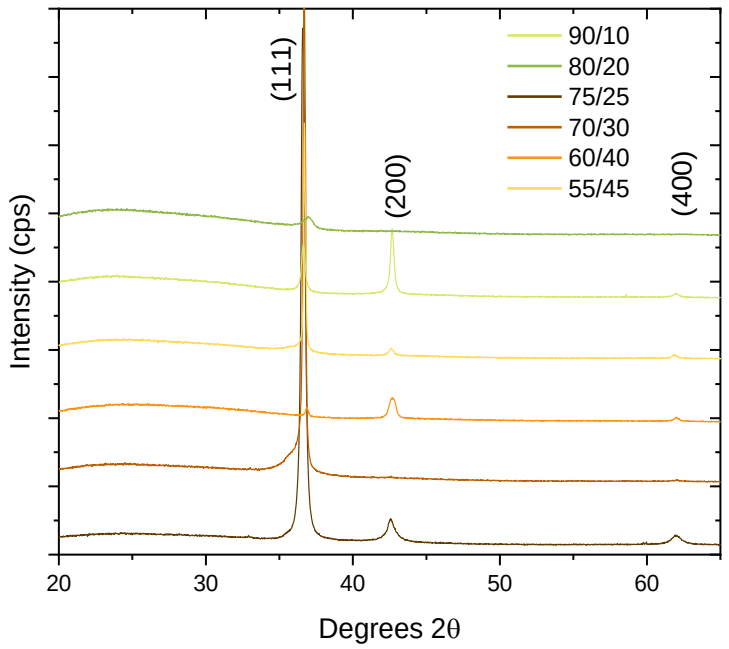

Figure 54 XRD peaks of TiN deposited on glass substrates under heating for different nitrogen compositions from 10% to 45%.

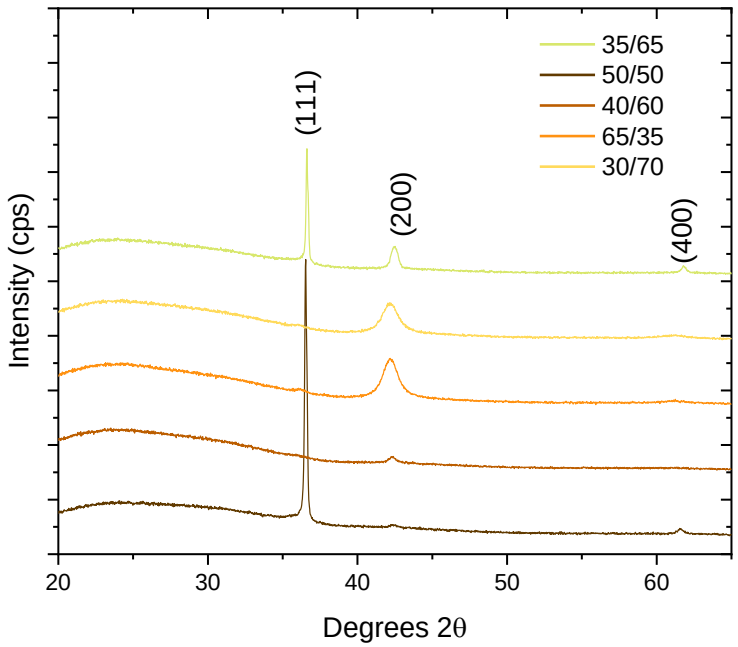

Figure 55 XRD peaks of TiN deposited on glass substrates under heating for different nitrogen compositions from 35% to 70%.

3.4.4 Raman Analysis for Samples Sputtered Under Substrate Heating

For silicon substrates first wo peaks stand between 250-400 cm^{-1} and 650-850 cm^{-1} being transverse acoustic and second order transverse acoustic. These peak positions and phonon names differ in variations of peak intensities and positions according to nitrogen amount. When the intensities of both silicon and glass substrates are compared, it can be easily observed the intensity 2TA of glass is higher than in silicon. With the increase in peak intensities, the phonons shift to right. The intensity of LA peak decreases with decreasing nitrogen partial pressure. Also, this could be due to the oxygen presence in the samples. One of the multiphonon peaks is shown on glass substrates LA+TO(800 cm^{-1}) can be seen in lower intensities and second-order 2TO(1100 cm^{-1}) is not available. Raman applied power of 5% was kept constant for these samples as in other sets and results showed TiN structures, due to the decreased oxygenation.

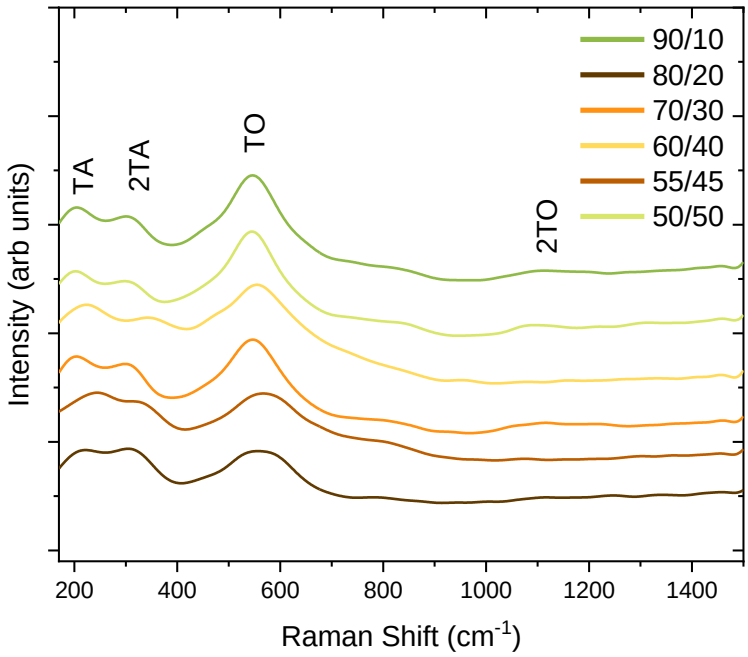

Figure 56 Raman spectra for samples deposited on silicon substrates under heating for varying nitrogen percentages from 10% to 50%.

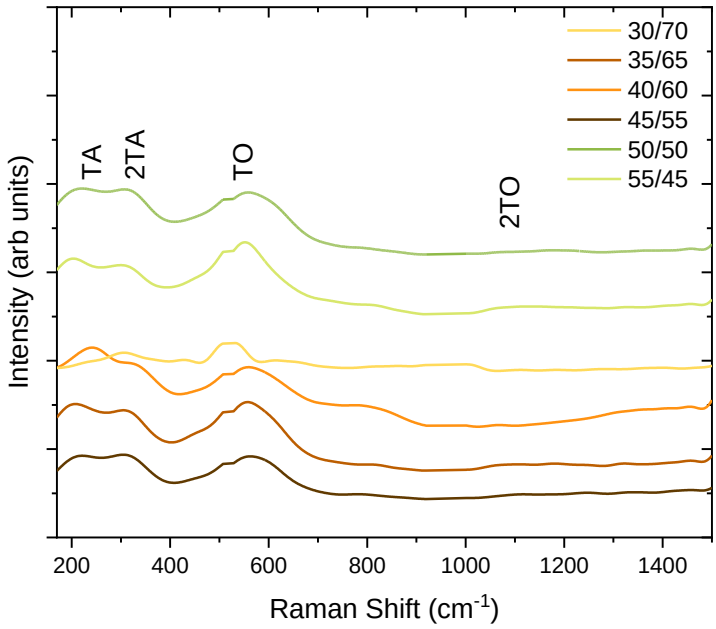

Figure 57 Raman spectra for samples deposited on silicon substrates under heating for varying nitrogen percentages from 45% to 70%.

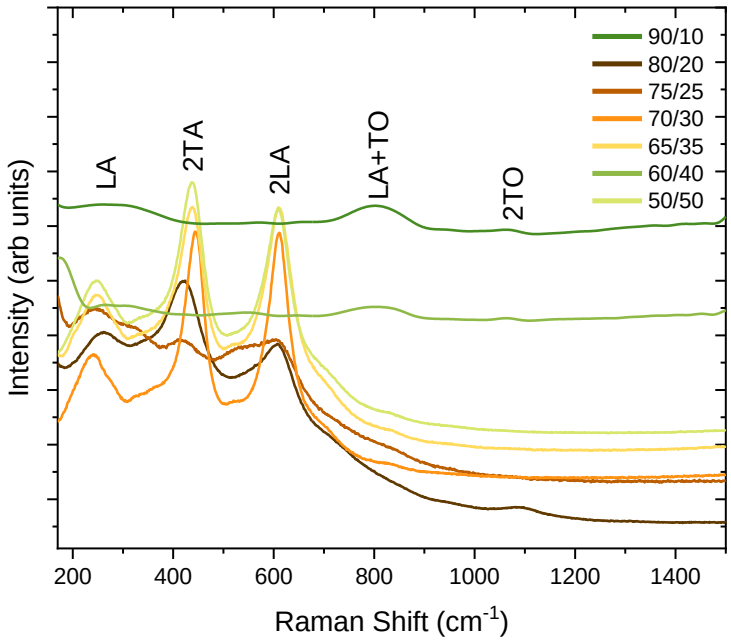

Figure 58 Raman spectra for samples deposited on glass substrates under heating for varying nitrogen compositions from 10% to 50%.

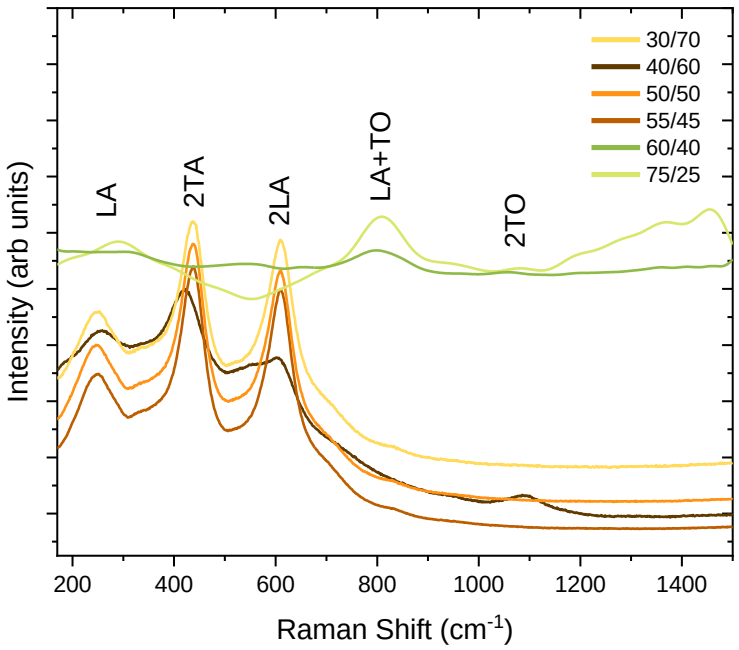

Figure 59 Raman spectra for samples deposited on glass substrates under heating for varying nitrogen compositions from 25% to 70%.

3.4.5 Four Point Probe Meaurement for Samples Sputtered Under Substrate Heating

Since, the current and voltage electrodes are separated, the four point probe can detect low resistances [87]. The impact of deposition pressure, nitrogen flow, and thin film composition, and structure was investigated in the sheet resistivity stability. According to the findings, low deposition pressure and heat resulted in thin films with a higher conductivity. For all samples, measurements are repeated 3 times from different parts of the substrates. Compared to other sets, these samples resulted conductive with the decrease in oxygen contamination.

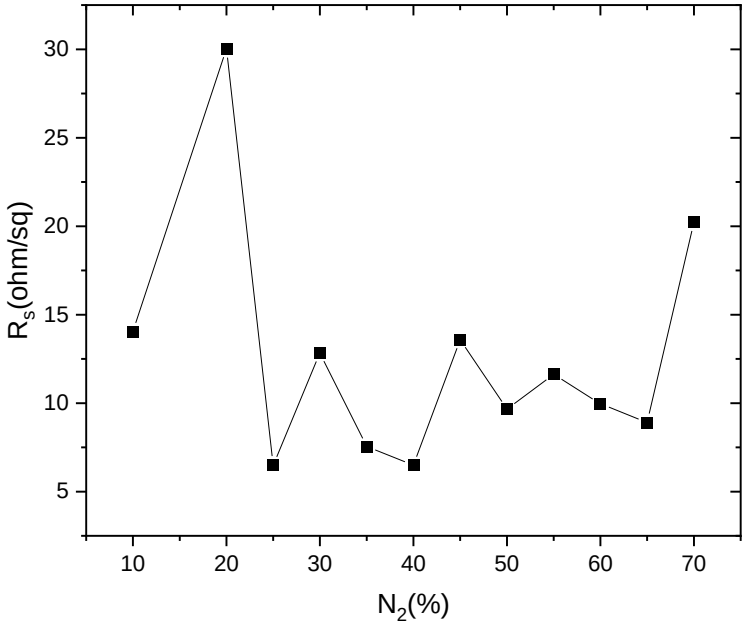

Figure 60 The measured sheet resistances of samples deposited on silicon under heating for different nitrogen partial pressures.

3.4.6 Optical Measurements for Samples Sputtered Under Substrate Heating

The real and imaginary part of the dielectric function, measured mostly in the range of angle of incidence 55°-75°, can be calculated from Fresnel equation and complex refractive index being $n' = n + ik$;

$$\rho = \frac{R_p}{R_s} = \tan(\psi) e^{i\Delta} \tag{3.1}$$

$$\varepsilon = sin^2\theta[1 + tan^2\varphi(\frac{1-\rho_f}{1+\rho_f})^2] \tag{3.2}$$

$$n = \frac{1-R}{1+R-2cos\theta\sqrt{R}}, \tag{3.3}$$

$$k = \frac{-2sin\theta\sqrt{R}}{1+R-2cos\theta\sqrt{R}}$$

$$\varepsilon_1 = n^2 - k^2, \varepsilon_2 = 2nk \tag{3.4}$$

The formulas above allow defining the metallic properties of the TiN thin film. The ε′ and ε″ values are illustrated as a function of the wavelength in Figure 61 and Figure 62, respectively. Plasmonic materials are defined with (3.4), and $\varepsilon = \varepsilon_1 + i\varepsilon_2$. These measurements were determined based on VASE results. The experimental data produced from the software WVASE32 gives the data by ψ(λ) and Δ(λ), obtained for three angles of incidence at 65°, 70°, and 75°. The conversion from psi and delta to real and imaginary parts are not direct. It needs to be fitted to a model of dielectric function which defines the material in interest. The fits were done on a model starting with silicon, SiO_2, and Lorentz Oscillator model with minimum mean square error. The Lorentz model explains the interband transitions of electrons from the valence band to conduction band. From the software Lorentz with four oscillators was applied, which means high energy transitions in interband. The number of oscillators mean the shift of peaks towards the beginning of visible region. Other sets could not be fitted with Lorentz since they showed the behavior of amorphous structures. The energy needed for electrons to jump upper states are high because the real part of the permittivity decreased to negative values, achieved within lowered oxygen impurity, and crystallinity improved. Our results show that within increasing content of nitrogen, negative real part is increasing. The low nitrogen content shows nearly dielectric profile. The trend is not consistent for 80/20 sample which is dielectric but overall, the conclusion is suitable. The 35/65 sample film presents the lowest real permittivity around $\varepsilon' \approx -30$ for $\lambda = 1700$ nm. After that, 30/70 has the second

lowest real permittivity around $\varepsilon' \approx -25$. Even though lowest real part appears with nitrogen-rich medium, the imaginary part is too high meaning they are subjected to high loss. The metallic property is often estimated using the absolute value of the real component of the permittivity (ε'), which must be as high as possible to be considered a good conductor like in Figure 63 gold (Au). Gold shows ε' around - 130 for $\lambda = 1700$ nm. For the imaginary part of permittivity, ε'' evolves nearly linear as a function of the wavelength up to $\varepsilon'' \approx 45$ in the range of 300 and 1700 nm. Imaginary part confirms the loss behavior of the TiN thin film. The imaginary part is not below 10, the samples that are close to 10 does not show reasonable plasmonic behavior.

As a result, from these ellipsometry analyses, compared with recent articles for plasmonic TiN [88], a lower performance metallic characteristic is observed because of high loss in the interband transitions. The sensitivity of TiN's optical property is affected by various factors such as stoichiometry, impurities like oxidation, grain size affecting the mean free path of conducting electrons, electron density. Also, this can be related to the conductivity as well. Overall, results prove that with the further studies TiN could be a potential for plasmonic applications in the regions of visible to NIR.

There has been a performance comparison of deposited layers of TiN and gold for localized surface plasmon resonance sensing (LSPR). In Figure 65 and Figure 66, figure of merit (FOM) is given. The high loss of TiN shows lower performance than Au. While Au showed considerably high performance ≈ 20, TiN responses highly low performance ≈ 0.8 due to their large loss in the imaginary part of their permittivities. The optical properties should be improved more to be tunable and competitive in nanoplasmonic sensing when compared with the noble metal.

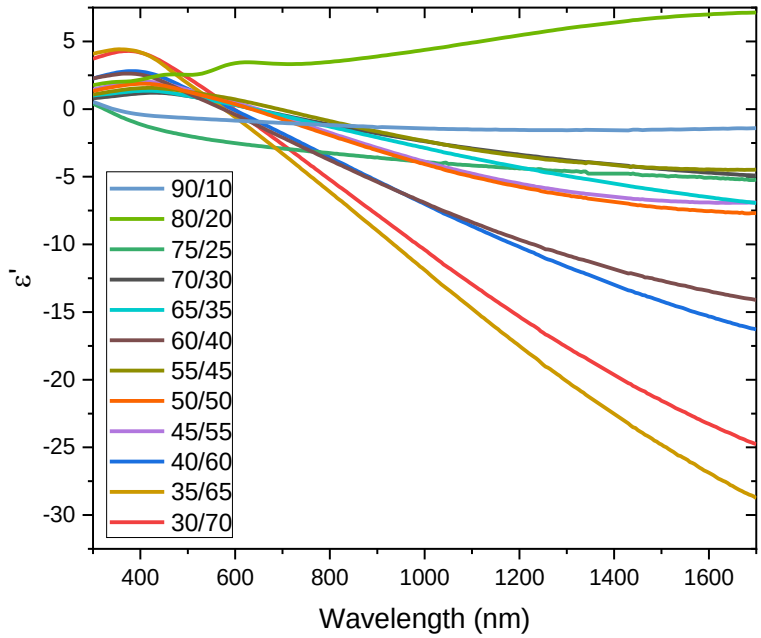

Figure 61 The real part of dielectic function for heated substrate -silicon samples from argon-rich to argon deficient ratios.

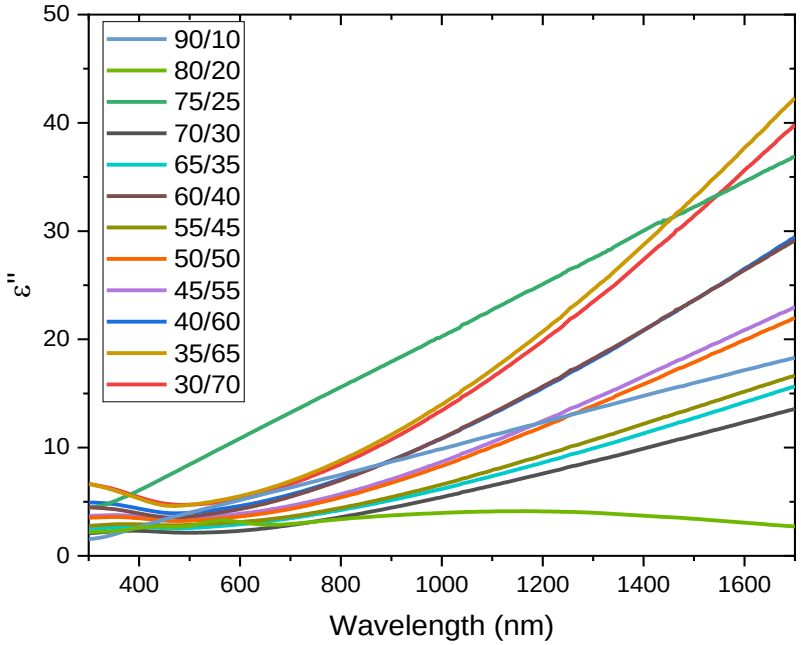

Figure 62 The imaginary part of dielectic function for heated substrate -silicon samples from argon-rich to argon deficient ratios.

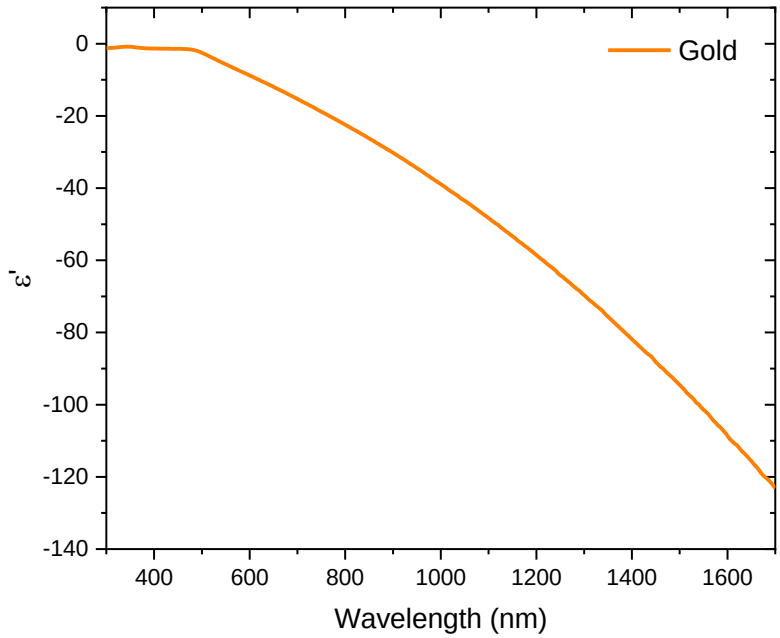

Figure 63 The real part of dielectic function for gold deposited silicon substrate.

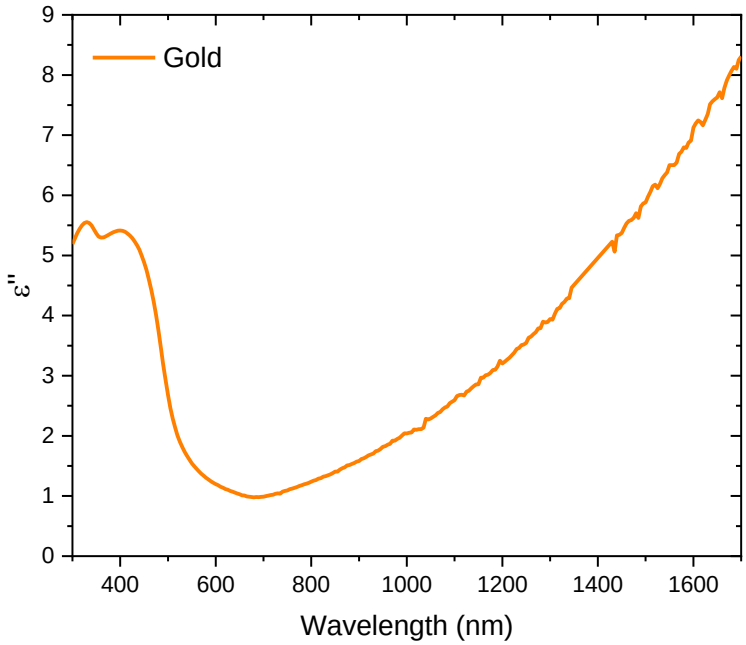

Figure 64 The imaginary part of dielectric function for gold deposited silicon substrate.

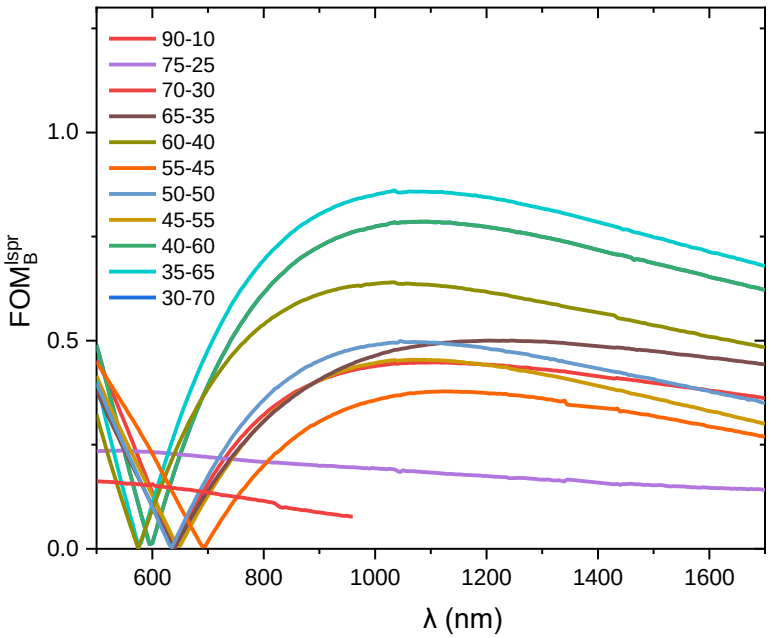

Figure 65 The bulk FoM of LSPR for TiN samples deposited under heating with various N_2 %.

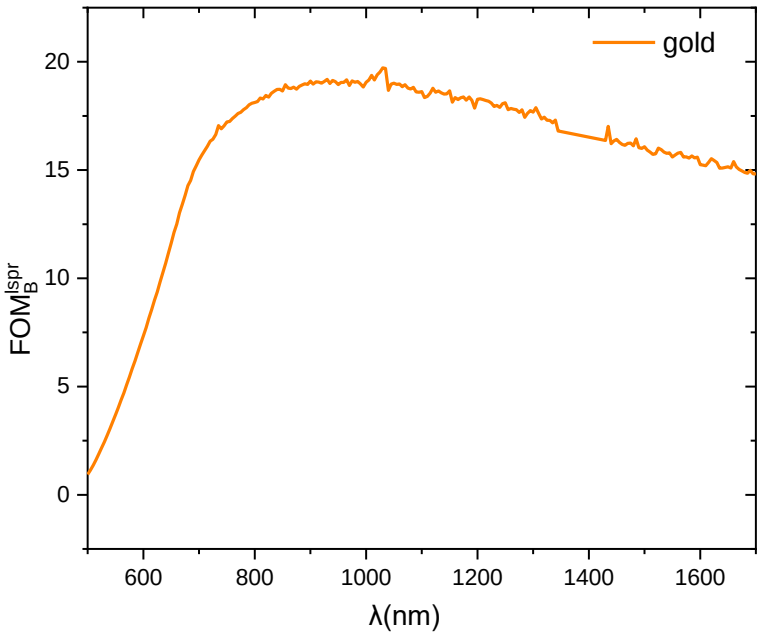

Figure 66 The calculated bulk FoM of LSPR for gold (Au).

4 Conclusion & Future Work

In this study, numerous approaches for reducing oxygen content in deposition and optimizing the Ar/N_2 ratio in reactive sputtering of TiN thin films were investigated, with the goal of developing nanoplasmonic biosensors. Various techniques and substrate types were used in these experiments. The impact of sputtering pressure and substrate heating on physical and electrical properties of the films, such as sheet resistance, crystallinity, and metal-like behavior, was studied.

As reported in the literature room-temperature sputtering was used for better stability and quality, also to promote fabrication of nanohole arrays using nanosphere lithography to protect polymer beads from ion bombardment in the chamber. However, the first set of EDS data revealed a high level of oxygen (80%), a different strategy was required to reduce contamination. Separately and in combination, argon gas purging for an hour and overnight vacuum were explored. There was not a noticable difference between these vaccum settings. Finally, prior zirconium cleaning and heating the substrates during deposition had a distinct influence on the quality, with oxygen levels dropping by about 60%. SEM-EDS, XRD, raman spectroscopy, and conductivity test with a 4-point probe were used to characterize all of these approaches. Only heated samples had the lowest resistance, which was evaluated with VASE to demonstrate plasmonic behavior. Overall, as the process is altered, the oxygen content of deposited TiN decreases. Sharp peaks were seen in XRD data as proof of crystalline TiN thin films when oxygen contamination was reduced and substrates were placed under heating.

The optical characteristics of nitrogen-rich samples were enhanced. Optical results, on the other hand, need to be investigated further. When compared to gold, our TiN exhibits substantial losses, with gold having $\varepsilon'' \approx 9$ and TiN having $\varepsilon'' \approx 40$. Performance comparison for LSPR concluded, it is highly dependent on the interband losses. Despite the fact that there are various discrete approaches for reducing oxygen content in thin film deposition as in the literature, this work showed the combined effect of lower pressure deposition, chamber purity, nitrogen partial pressure, and high substrate temperature effects in a systematic way. It was found that pre-cleaning and heating the chamber strongly affected the coating character. Furthermore, it is possible to tune the texture of

TiN thin films by deposition temperature and changing nitrogen to argon ratio. For the future work, sputtering with DC magnetrons and annealling thin film will be tried to reduce the ignition and deposition time, and to obtain better crystallinity. In RF magnetron, it takes longer time to ignite plasma, so the system has more time to leak oxygen into the system. This study is just the beginning for the production of PoC nanoplasmonic biosensors with titanium nitride and I hope more research will be made to overcome disadvantages in this field.

REFERENCES

[1] R. T. Hill, "Plasmonic biosensors," *Wiley Interdisciplinary Reviews: Nanomedicine and Nanobiotechnology*, vol. 7, no. 2, pp. 152–168, 2015, doi: 10.1002/wnan.1314.

[2] A. Csáki, O. Stranik, and W. Fritzsche, *Localized surface plasmon resonance based biosensing*, vol. 18, no. 3. 2018. doi: 10.1080/14737159.2018.1440208.

[3] B. Menges, "Surface Plasmon and Optical Waveguide Fluorescence Spectroscopy in Limit of Surface Plasmon Fluorescence Spectroscopy and Optical Waveguide Fluorescence Spectroscopy in Limit of Detection Studies Master Thesis Akihiro Sato Department of Information Proces," no. April, 2015, doi: 10.1002/1616-3028(20020916).

[4] H. Kurt *et al.*, "Nanoplasmonic biosensors: Theory, structure, design, and review of recent applications," *Analytica Chimica Acta*, no. xxxx, 2021, doi: 10.1016/j.aca.2021.338842.

[5] K. Takagi, S. v. Nair, R. Watanabe, K. Seto, T. Kobayashi, and E. Tokunaga, "Surface plasmon polariton resonance of gold, silver, and copper studied in the kretschmann geometry: Dependence on wavelength, angle of incidence, and film thickness," *Journal of the Physical Society of Japan*, vol. 86, no. 12, 2017, doi: 10.7566/JPSJ.86.124721.

[6] S. S. Hinman, K. S. McKeating, and Q. Cheng, "Surface Plasmon Resonance: Material and Interface Design for Universal Accessibility," *Analytical Chemistry*, vol. 90, no. 1, pp. 19–39, 2018, doi: 10.1021/acs.analchem.7b04251.

[7] Y. Lee, J. Kim, S. Sim, I. Llamas-Garro, and J. Kim, "Air-gap interrogation of surface plasmon resonance in otto configuration," *Micromachines*, vol. 12, no. 8, pp. 2–11, 2021, doi: 10.3390/mi12080998.

[8] Y. Sonnefraud, A. L. Leen Koh, D. W. McComb, and S. A. Maier, "Nanoplasmonics: Engineering and observation of localized plasmon modes," *Laser and Photonics Reviews*, vol. 6, no. 3, pp. 277–295, 2012, doi: 10.1002/lpor.201100027.

[9] S. Unser, I. Bruzas, J. He, and L. Sagle, “Localized surface plasmon resonance biosensing: Current challenges and approaches,” *Sensors (Switzerland)*, vol. 15, no. 7, pp. 15684–15716, 2015, doi: 10.3390/s150715684.

[10] A. v. Zayats, I. I. Smolyaninov, and A. A. Maradudin, “Nano-optics of surface plasmon polaritons,” *Physics Reports*, vol. 408, no. 3–4, pp. 131–314, 2005, doi: 10.1016/j.physrep.2004.11.001.

[11] X. Zhou *et al.*, “In Situ Synthesis of Metal Nanoparticles on Single-Layer Graphene Oxide and Reduced Graphene Oxide Surfaces,” vol. 113, pp. 10842–10846, 2009, doi: 10.1021/jp903821n.

[12] J. A. Jackman, A. Rahim Ferhan, and N. J. Cho, “Nanoplasmonic sensors for biointerfacial science,” *Chemical Society Reviews*, vol. 46, no. 12, pp. 3615–3660, 2017, doi: 10.1039/c6cs00494f.

[13] G. A. Lopez, M. C. Estevez, M. Soler, and L. M. Lechuga, “Recent advances in nanoplasmonic biosensors: Applications and lab-on-a-chip integration,” *Nanophotonics*, vol. 6, no. 1, pp. 123–136, 2017, doi: 10.1515/nanoph-2016-0101.

[14] M. C. Estevez, M. A. Otte, B. Sepulveda, and L. M. Lechuga, “Trends and challenges of refractometric nanoplasmonic biosensors: A review,” *Analytica Chimica Acta*, vol. 806, pp. 55–73, 2014, doi: 10.1016/j.aca.2013.10.048.

[15] J. X. Cao, X. J. Zhang, and D. Q. Geng, “Extraordinaryoptical transmissionthrough sub-wavelengthhole arrays,” *Journal of Clinical Neurology*, vol. 23, no. 6, pp. 414–416, 2010.

[16] D. P. Langley, E. Balaur, Y. Hwang, C. Sadatnajafi, and B. Abbey, “Optical Chemical Barcoding Based on Polarization Controlled Plasmonic Nanopixels,” *Advanced Functional Materials*, vol. 28, no. 4, 2018, doi: 10.1002/adfm.201704842.

[17] P. R. West, S. Ishii, G. v. Naik, N. K. Emani, V. M. Shalaev, and A. Boltasseva, “Searching for better plasmonic materials,” *Laser and Photonics Reviews*, vol. 4, no. 6, pp. 795–808, 2010, doi: 10.1002/lpor.200900055.

[18] P. K. Jain and M. A. El-Sayed, “Plasmonic coupling in noble metal nanostructures,” *Chemical Physics Letters*, vol. 487, no. 4–6, pp. 153–164, 2010, doi: 10.1016/j.cplett.2010.01.062.

[19] V. Giannini, A. I. Fernández-Domínguez, S. C. Heck, and S. A. Maier, “Plasmonic nanoantennas: Fundamentals and their use in controlling the radiative properties

of nanoemitters," *Chemical Reviews*, vol. 111, no. 6, pp. 3888–3912, 2011, doi: 10.1021/cr1002672.

[20] P. B. Johnson and R. W. Christy, "Optical Constant of the Nobel Metals," *Physical Review B*, vol. 6, no. 12, pp. 4370–4379, 1972.

[21] J. Liu, M. Jalali, S. Mahshid, and S. Wachsmann-Hogiu, "Are plasmonic optical biosensors ready for use in point-of-need applications?," *Analyst*, vol. 145, no. 2, pp. 364–384, 2020, doi: 10.1039/c9an02149c.

[22] T. Maurer *et al.*, "Enhancing LSPR Sensitivity of Au Gratings through Graphene Coupling to Au Film," *Plasmonics*, vol. 9, no. 3, pp. 507–512, 2014, doi: 10.1007/s11468-013-9649-0.

[23] S. Baldelli, A. S. Eppler, E. Anderson, Y. R. Shen, and G. A. Somorjai, "Surface enhanced sum frequency generation of carbon monoxide adsorbed on platinum nanoparticle arrays," *Journal of Chemical Physics*, vol. 113, no. 13, pp. 5432–5438, 2000, doi: 10.1063/1.1290024.

[24] F. Sterl, N. Strohfeldt, R. Walter, R. Griessen, A. Tittl, and H. Giessen, "Magnesium as novel material for active plasmonics in the visible wavelength range," *Nano Letters*, vol. 15, no. 12, pp. 7949–7955, 2015, doi: 10.1021/acs.nanolett.5b03029.

[25] M. Lee *et al.*, "Aluminum Nanoarrays for Plasmon-Enhanced Light Harvesting," *ACS Nano*, vol. 9, no. 6, pp. 6206–6213, 2015, doi: 10.1021/acsnano.5b01541.

[26] B. Doiron *et al.*, "Quantifying Figures of Merit for Localized Surface Plasmon Resonance Applications: A Materials Survey," *ACS Photonics*, vol. 6, no. 2, pp. 240–259, 2019, doi: 10.1021/acsphotonics.8b01369.

[27] G. v. Naik, V. M. Shalaev, and A. Boltasseva, "Alternative Plasmonic Materials: Beyond Gold and Silver," *Advanced Materials*, vol. 25, no. 24, pp. 3264–3294, Jun. 2013, doi: 10.1002/adma.201205076.

[28] P. Patsalas, N. Kalfagiannis, and S. Kassavetis, "Optical Properties and Plasmonic Performance of Titanium Nitride," *Materials*, vol. 8, no. 6, pp. 3128–3154, May 2015, doi: 10.3390/ma8063128.

[29] G. v. Naik, J. Kim, and A. Boltasseva, "Oxides and nitrides as alternative plasmonic materials in the optical range [Invited]," *Optical Materials Express*, vol. 1, no. 6, p. 1090, Oct. 2011, doi: 10.1364/OME.1.001090.

[30] P. Patsalas, N. Kalfagiannis, and S. Kassavetis, “Optical Properties and Plasmonic Performance of Titanium Nitride,” *Materials*, vol. 8, no. 6, pp. 3128–3154, May 2015, doi: 10.3390/ma8063128.

[31] P. Patsalas *et al.*, “Conductive nitrides: Growth principles, optical and electronic properties, and their perspectives in photonics and plasmonics,” *Materials Science and Engineering: R: Reports*, vol. 123, pp. 1–55, Jan. 2018, doi: 10.1016/J.MSER.2017.11.001.

[32] S. Paik *et al.*, “Near-field sub-diffraction photolithography with an elastomeric photomask,” *Nature Communications*, vol. 11, no. 1, pp. 1–13, 2020, doi: 10.1038/s41467-020-14439-1.

[33] J. S. Wi *et al.*, “Fabrication of silicon nanopillar teradot arrays by electron-beam patterning for nanoimprint molds,” *Small*, vol. 4, no. 12, pp. 2118–2122, 2008, doi: 10.1002/smll.200800625.

[34] J. F. Masson, “Surface Plasmon Resonance Clinical Biosensors for Medical Diagnostics,” *ACS Sensors*, vol. 2, no. 1, pp. 16–30, 2017, doi: 10.1021/acssensors.6b00763.

[35] N. A. Cinel, S. Bütün, and E. Özbay, “Electron beam lithography designed silver nano-disks used as label free nano-biosensors based on localized surface plasmon resonance,” *Optics Express*, vol. 20, no. 3, p. 2587, 2012, doi: 10.1364/oe.20.002587.

[36] T. W. Ebbesen, H. J. Lezec, H. F. Ghaemi, T. Thio, and P. A. Wolff, “Extraordinary optical transmission through sub-wavelenght hole arrays,” *Nature*, vol. 391, no. 6668, pp. 667–669, 1998, doi: 10.1038/35570.

[37] M. E. Stewart *et al.*, “Nanostructured plasmonic sensors,” *Chemical Reviews*, vol. 108, no. 2, pp. 494–521, 2008, doi: 10.1021/cr068126n.

[38] N. C. Lindquist, P. Nagpal, K. M. McPeak, D. J. Norris, and S. H. Oh, “Engineering metallic nanostructures for plasmonics and nanophotonics,” *Reports on Progress in Physics*, vol. 75, no. 3, 2012, doi: 10.1088/0034-4885/75/3/036501.

[39] M. B. T.-F. and A. of N. S. in P. and F. Nayfeh, Ed., “Chapter 5 - Manipulation and Patterning of Surfaces (Nanolithography),” in *Micro and Nano Technologies*, Elsevier, 2018, pp. 89–137. doi: https://doi.org/10.1016/B978-0-323-48057-4.00005-0.

[40] R. Luttge, “Chapter 4 - Nanotechnology,” in *Micro and Nano Technologies*, R. B. T.-M. for I. A. Luttge, Ed. Boston: William Andrew Publishing, 2011, pp. 91–146. doi: https://doi.org/10.1016/B978-0-8155-1582-1.00004-6.

[41] K. Seshan, *Handbook of Thin-Film Deposition Processes and Techniques*, Second edi. Noyes Publication, 2002. doi: 2001135178.

[42] P. Zheng, S. K. Cushing, S. Suri, and N. Wu, “Tailoring plasmonic properties of gold nanohole arrays for surface-enhanced Raman scattering,” *Physical Chemistry Chemical Physics*, vol. 17, no. 33, pp. 21211–21219, 2015, doi: 10.1039/c4cp05291a.

[43] I. Mínguez-Bacho, F. Scheler, P. Büttner, K. Bley, N. Vogel, and J. Bachmann, “Ordered nanopore arrays with large interpore distances: Via one-step anodization,” *Nanoscale*, vol. 10, no. 18, pp. 8385–8390, 2018, doi: 10.1039/c8nr02215a.

[44] A. Manuscript, “Nanodevices in diagnostics,” pp. 1–35, 2011, doi: 10.1002/wnan.82.Nanodevices.

[45] X. Li, M. Soler, C. I. Özdemir, A. Belushkin, F. Yesilköy, and H. Altug, “Plasmonic nanohole array biosensor for label-free and real-time analysis of live cell secretion,” *Lab on a Chip*, vol. 17, no. 13, pp. 2208–2217, 2017, doi: 10.1039/c7lc00277g.

[46] S. M. Fothergill, C. Joyce, and F. Xie, “Metal enhanced fluorescence biosensing: From ultra-violet towards second near-infrared window,” *Nanoscale*, vol. 10, no. 45, pp. 20914–20929, 2018, doi: 10.1039/c8nr06156d.

[47] J. A. Goode, J. V. H. Rushworth, and P. A. Millner, “Biosensor Regeneration: A Review of Common Techniques and Outcomes,” *Langmuir*, vol. 31, no. 23, pp. 6267–6276, 2015, doi: 10.1021/la503533g.

[48] N. Bhalla, P. Jolly, N. Formisano, and P. Estrela, “Introduction to biosensors,” *Essays in Biochemistry*, vol. 60, no. 1, pp. 1–8, 2016, doi: 10.1042/EBC20150001.

[49] S. Sang, Y. Wang, Q. Feng, Y. Wei, J. Ji, and W. Zhang, “Progress of new label-free techniques for biosensors: A review,” *Critical Reviews in Biotechnology*, vol. 36, no. 3, pp. 465–481, 2016, doi: 10.3109/07388551.2014.991270.

[50] H. H. Nguyen, J. Park, S. Kang, and M. Kim, “Surface plasmon resonance: A versatile technique for biosensor applications,” *Sensors (Switzerland)*, vol. 15, no. 5, pp. 10481–10510, 2015, doi: 10.3390/s150510481.

[51] D. A. Hall, J. Ptacek, and M. Snyder, “Protein microarray technology,” *Mechanisms of Ageing and Development*, vol. 128, no. 1, pp. 161–167, 2007, doi: 10.1016/j.mad.2006.11.021.

[52] N. Lévêque, F. Renois, and L. Andréoletti, “The microarray technology: Facts and controversies,” *Clinical Microbiology and Infection*, vol. 19, no. 1, pp. 10–14, 2013, doi: 10.1111/1469-0691.12024.

[53] M. J. Heller, “DNA microarray technology: Devices, systems, and applications,” *Annual Review of Biomedical Engineering*, vol. 4, pp. 129–153, 2002, doi: 10.1146/annurev.bioeng.4.020702.153438.

[54] V. Gubala, L. F. Harris, A. J. Ricco, M. X. Tan, and D. E. Williams, “Point of care diagnostics: Status and future,” *Analytical Chemistry*, vol. 84, no. 2, pp. 487–515, 2012, doi: 10.1021/ac2030199.

[55] S. Nayak, N. R. Blumenfeld, T. Laksanasopin, and S. K. Sia, “POC Diagnostics: Recent Devs in a Connected Age,” *Physiology & behavior*, vol. 176, no. 1, pp. 139–148, 2018, doi: 10.1021/acs.analchem.6b04630.Point-of-Care.

[56] D. R. Thvenot, K. Toth, R. A. Durst, and G. S. Wilson, “Electrochemical biosensors: Recommended definitions and classification (Technical Report),” *Pure and Applied Chemistry*, vol. 71, no. 12, pp. 2333–2348, 1999, doi: 10.1351/pac199971122333.

[57] D. Grieshaber, R. MacKenzie, J. Vörös, and E. Reimhult, “Electrochemical biosensors - Sensor principles and architectures,” *Sensors*, vol. 8, no. 3, pp. 1400–1458, 2008, doi: 10.3390/s8031400.

[58] M. Calleja, P. M. Kosaka, Á. San Paulo, and J. Tamayo, “Challenges for nanomechanical sensors in biological detection,” *Nanoscale*, vol. 4, no. 16, pp. 4925–4938, 2012, doi: 10.1039/c2nr31102j.

[59] N. Sabri, S. A. Aljunid, M. S. Salim, R. B. Ahmad, and R. Kamaruddin, “Toward optical sensors: Review and applications,” *Journal of Physics: Conference Series*, vol. 423, no. 1, 2013, doi: 10.1088/1742-6596/423/1/012064.

[60] H. N. Daghestani and B. W. Day, “Theory and applications of surface plasmon resonance, resonant mirror, resonant waveguide grating, and dual polarization interferometry biosensors,” *Sensors*, vol. 10, no. 11, pp. 9630–9646, 2010, doi: 10.3390/s101109630.

[61] J. R. Mejía-Salazar and O. N. Oliveira, “Plasmonic Biosensing,” *Chemical Reviews*, vol. 118, no. 20, pp. 10617–10625, 2018, doi: 10.1021/acs.chemrev.8b00359.

[62] M. Retsch *et al.*, “Fabrication of Large-Area, Transferable Colloidal Monolayers Utilizing Self-Assembly at the Air/Water Interface,” *Macromolecular Chemistry and Physics*, vol. 210, no. 3–4, pp. 230–241, Feb. 2009, doi: 10.1002/macp.200800484.

[63] C. P. P. Jr. Frank J. Owens, *The Physics and Chemistry of Nanosolids*. USA, 2008.

[64] Z. Wang, B. Ai, H. Möhwald, and G. Zhang, “Colloidal Lithography Meets Plasmonic Nanochemistry,” *Advanced Optical Materials*, vol. 6, no. 18, pp. 1–18, 2018, doi: 10.1002/adom.201800402.

[65] M. H. Kim, W. S. Kang, and J. D. Kim, “Two dimensional template of polystyrene latex as an alignment layer of liquid crystals,” *Molecular Crystals and Liquid Crystals Science and Technology Section A: Molecular Crystals and Liquid Crystals*, vol. 349, pp. 127–130, 2000, doi: 10.1080/10587250008024882.

[66] A. S. Bhurke, P. A. Askeland, and L. T. Drzal, “Surface modification of polycarbonate by ultraviolet radiation and ozone,” *Journal of Adhesion*, vol. 83, no. 1, pp. 43–66, Jan. 2007, doi: 10.1080/00218460601102860.

[67] Sina Ebnesajjad, *Surface Treatment of Materials for Adhesive Bonding Surface Treatment of Materials for Adhesive Bonding*. 2014.

[68] M. Aliofkhazraei and N. Ali, *PVD Technology in Fabrication of Micro- and Nanostructured Coatings*, vol. 7. Elsevier, 2014. doi: 10.1016/B978-0-08-096532-1.00705-6.

[69] A. Bashir, T. I. Awan, A. Tehseen, M. B. Tahir, and M. Ijaz, “Chapter 3 - Interfaces and surfaces,” T. I. Awan, A. Bashir, and A. B. T.-C. of N. Tehseen, Eds. Elsevier, 2020, pp. 51–87. doi: https://doi.org/10.1016/B978-0-12-818908-5.00003-2.

[70] R. J. Martín-Palma and A. Lakhtakia, “Chapter 15 - Vapor-Deposition Techniques,” A. Lakhtakia and R. J. B. T.-E. B. Martín-Palma, Eds. Boston: Elsevier, 2013, pp. 383–398. doi: https://doi.org/10.1016/B978-0-12-415995-2.00015-5.

[71] O. O. Abegunde, E. T. Akinlabi, O. P. Oladijo, S. Akinlabi, and A. U. Ude, “Overview of thin film deposition techniques,” *AIMS Materials Science*, vol. 6, no. 2, pp. 174–199, 2019, doi: 10.3934/MATERSCI.2019.2.174.

[72] S. P. Tallósy, L. Janovák, E. Nagy, and I. Dékány, “Preparation and Antibacterial Properties of Reactive Surface Coatings Using Solar Energy Driven Photocatalyst,” *Handbook of Antimicrobial Coatings*, pp. 89–107, Jan. 2018, doi: 10.1016/B978-0-12-811982-2.00005-6.

[73] J. I. Goldstein, D. E. Newbury, J. R. Michael, N. W. M. Ritchie, J. H. J. Scott, and D. C. Joy, *Microscopy and X-Ray Microanalysis*. 2018.

[74] A. D. Weiss, “Scanning Electron Microscopes.,” *Semiconductor International*, vol. 6, no. 10, pp. 90–94, 1983, doi: 10.1016/s0026-0576(03)90123-1.

[75] J. A. Woollam, B. D. Johs, C. M. Herzinger, J. N. Hilfiker, R. A. Synowicki, and C. L. Bungay, “Overview of variable-angle spectroscopic ellipsometry (VASE): I. Basic theory and typical applications,” *Optical Metrology: A Critical Review*, vol. 10294. p. 1029402, 1999. doi: 10.1117/12.351660.

[76] M. Naftaly *et al.*, “Sheet resistance measurements of conductive thin films: A comparison of techniques,” *Electronics (Switzerland)*, vol. 10, no. 8, 2021, doi: 10.3390/electronics10080960.

[77] M. Sain, S. Ummartyotin, J. Juntaro, C. Wu, and H. Manuspiya, “Deposition of PEDOT: PSS nanoparticles as a conductive microlayer anode in OLEDs device by desktop inkjet printer,” *Journal of Nanomaterials*, vol. 2011, 2011, doi: 10.1155/2011/606714.

[78] A. M. Mahros and M. M. Tharwat, “Investigating the fabrication imperfections of plasmonic nanohole arrays and its effect on the optical transmission spectra,” *Journal of Nanomaterials*, vol. 2015, 2015, doi: 10.1155/2015/178583.

[79] M. Ohring, “Chapter 1 - A Review of Materials Science,” M. B. T.-M. S. of T. F. (Second E. Ohring, Ed. San Diego: Academic Press, 2002, pp. 1–56. doi: https://doi.org/10.1016/B978-012524975-1/50004-5.

[80] S. v. Rempel, A. A. Rempel, and A. A. Valeeva, “Effect of Stoichiometry and Ordering on the Microstructure of Titanium Monoxide TiOy,” *ACS Omega*, vol. 5, no. 35, pp. 22513–22519, 2020, doi: 10.1021/acsomega.0c03122.

[81] K. S. Nithin, K. N. Shilpa, R. Thimmaiah, B. M. Jagajeevan Raj, S. Sachhidananda, and H. Siddaramaiah, “Tools and techniques toward characterizing polymer-based smart composites for optical, optoelectronic, and energy-related applications,” *Polymer-Based Advanced Functional Composites for Optoelectronic and Energy Applications*, pp. 91–115, Jan. 2021, doi: 10.1016/B978-0-12-818484-4.00012-4.

[82] M. A. Afifi, M. M. Abdel-Aziz, I. S. Yahia, M. Fadel, and L. A. Wahab, “Transport properties of polycrystalline TiO2 and Ti2O3 as semiconducting oxides,” *Journal of Alloys and Compounds*, vol. 455, no. 1–2, pp. 92–97, 2008, doi: 10.1016/j.jallcom.2007.01.156.

[83] D. Wang, C. Huang, J. He, X. Che, H. Zhang, and F. Huang, “Enhanced Superconductivity in Rock-Salt TiO,” *ACS Omega*, vol. 2, no. 3, pp. 1036–1039, 2017, doi: 10.1021/acsomega.7b00048.

[84] J. Jagannadham, K., Chowdhury, R., Biunno, N., & Narayan, “Raman Spectroscopy of Tin Films Deposited on Silicon (001) Substrate by Laser Physical Vapor Deposition,” *MRS Proceedings*, vol. 317, 1993, doi: doi:10.1557/proc-317-193.

[85] X. Y. Li *et al.*, “Observation of High-Frequency Transverse Phonons in Metallic Glasses,” *Physical Review Letters*, vol. 124, no. 22, pp. 1–6, 2020, doi: 10.1103/PhysRevLett.124.225902.

[86] H. Windischmann, “Intrinsic stress in sputter-deposited thin films,” *Critical Reviews in Solid State and Materials Sciences*, vol. 17, no. 6, pp. 547–596, Jan. 1992, doi: 10.1080/10408439208244586.

[87] V. M. Airaksinen, “Silicon Wafer and Thin Film Measurements,” *Handbook of Silicon Based MEMS Materials and Technologies: Second Edition*, pp. 381–390, Jan. 2015, doi: 10.1016/B978-0-323-29965-7.00015-4.

[88] H. Reddy, U. Guler, Z. Kudyshev, A. v. Kildishev, V. M. Shalaev, and A. Boltasseva, “Temperature-Dependent Optical Properties of Plasmonic Titanium Nitride Thin Films,” *ACS Photonics*, vol. 4, no. 6, pp. 1413–1420, 2017, doi: 10.1021/acsphotonics.7b00127.